JGR Solid Earth

RESEARCH ARTICLE
10.1029/2019JB017339

Special Section:
Physical Properties of Rocks, Friction and Fracturing: The Walsh Volume

Variations in Elastic and Electrical Properties of Crustal Rocks With Varying Degree of Microfracturation

L. Pimienta[1], L. F. Orellana[1,2], and M. Violay[1]

[1]Laboratory of Experimental Rock Mechanics, Ecole Polytechnique Fédérale de Lausanne, Lausanne, Switzerland, [2]Now at the Department of Mining Engineering, FCFM, Universidad de Chile, Santiago, Chile

Abstract This work aims at investigating the effect of varying degrees of microfracturing on the joint elastic and electrical transport properties of rocks. Different crustal rocks were subjected to thermal treatment, expected to induce microfracturing, up to different target temperatures from 100 up to 900 °C. The rocks bulk and pore volumes, *P* and *S* wave velocities, and frequency-dependent electrical impedance were measured before and after the treatment. As the temperature of treatment increased, *P* and *S* wave velocities and the electrical formation factor drop and pore and bulk volumes increase. As indicated by the microscopic images, this is consistent with the creation of microcracks. These created microcracks do not affect the properties in the exact same manner, and a strong effect of the initial porosity is observed for electrical formation factor. Extrapolating to low-frequency field-scale measurements in water-saturated reservoir rocks highlights an interesting observation: Both seismic and electrical properties at the field scale might highlight similar variations with increasing damage in all rocks. The maximum amount of decrease expected for all rocks is about 1 order of magnitude in electrical formation factor and 40% decrease in *P* and *S* wave velocities. Finally, temperature proved to affect very differently the rocks of varying porosity and mineral content, in ways not fully covered by existing works. Porosity, by increasing the matrix compressibility, damps the degree of microfracturing and crack opening. The distinct behavior in calcite-pure marble evidences a dominance of anisotropic of thermal expansion over isotropic expansion mismatch.

Key Points:
- Thermal treatments to investigate effects of varying microfracturing in rocks under ambient pressure conditions
- Large variations in elastic and electrical properties, dependent on rock initial porosity, mostly dominated by crack density over aperture
- Large difference between quartz- and calcite-rich rocks, indicating little effect of isotropic thermal expansion mismatch

Supporting Information:
- Supporting Information S1
- Data Set S1
- Data Set S2
- Data Set S3
- Data Set S4
- Data Set S5
- Data Set S6

Correspondence to:
L. Pimienta,
lucas.pimienta@epfl.ch

Citation:
Pimienta, L., Orellana, L. F., & Violay, M. (2019). Variations in elastic and electrical properties of crustal rocks with varying degree of microfracturation. *Journal of Geophysical Research: Solid Earth*, *124*, 6376–6396. https://doi.org/10.1029/2019JB017339

Received 9 JAN 2019
Accepted 28 MAY 2019
Accepted article online 4 JUN 2019
Published online 10 JUL 2019

1. Introduction

Over the last decades, field seismics and electrical resistivity have been acknowledged as powerful geophysical tools to characterize in situ reservoir rocks and monitor their evolution (Archie, 1941, 1952; Eberhart-Phillips et al., 1995; Knight et al., 2010; Knight & Dvorkin, 1992; Slater & Lesmes, 2002). Seismics allows characterizing fluid-saturated rocks from their effective stiffness, which links to its mineralogy and the amount and geometry of pore space and—for sedimentary rocks—to their degree of cement (Brace, 1965a; Guéguen & Kachanov, 2011; Guéguen & Palciauskas, 1994; Mavko et al., 2003; Simmons & Brace, 1965). However, alone, field seismics does not allow characterizing precisely the amount of saturation, the nature of fluid present in the rocks, and the reservoir hydraulic conductivity (Guéguen & Dienes, 1989; Guéguen & Palciauskas, 1994; Mavko et al., 2003). To complement this method, electrical resistivity is of great interest. In rocks of low mineral/intrinsic electrical conductivity, electrical conductivity originates from the presence of a conductive fluid within the pore network (e.g., Glover et al., 2000; Sen, 1997). If the fluid is conductive, the property depends on the topology of the pore network in a way very similar to that of hydraulic conductivity (Bernabé, 1991; Brace et al., 1965; Guéguen & Dienes, 1989; Walsh & Brace, 1984).

For fields with interest on geoengineering applications, because most reservoir rocks were sedimentary, extensive studies were aimed at unraveling the link between the fluid transport and acoustic properties in very porous and permeable rocks (e.g., Bernabé, 1991; Cai et al., 2017; Casteleyn et al., 2011; M. Han et al., 2009; Han, 2018; Han, Best, Sothcott, et al., 2011; Revil, 2013; Revil et al., 2014). For fields with interest on deeper solid earth—and on low-porosity rocks—emphasis was mostly given to hydraulic transport, elastic and mechanical properties (Benson et al., 2006; Brace et al., 1968; Faoro et al., 2013; Nara et al., 2011; Nasseri et al., 2007, 2009; Reuschlé et al., 2003; Schubnel et al., 2006; Vinciguerra et al., 2005; Walsh & Brace, 1984; Wang et al., 2013; Zhang et al., 2017), but little was done on the investigation of their electrical properties (Brace, 1977; Brace et al., 1965). With the new development of high-temperature/enthalpy geothermal energy, low-porosity and permeability crustal rocks such as granites become renewed

prospects, which field-scale properties need to be monitored when affected by varying degrees of microfracturing.

Because the applied pressures affect mostly the opening/closure of existing microfractures (e.g., Walsh, 1965a, 1965ab), the effect of a crack population on rocks effective properties is usually investigated under varying pressure conditions (Brace et al., 1968; Simmons & Brace, 1965; Walsh, 1965a, 1965ab, 1965ac). However, such studies involve the technical challenge of a triaxial apparatus able to measure rock properties at elevated pressures, which have been extensively developed to study mechanical, elastic, or hydraulic properties. Yet, much less apparatuses allow studying the evolution of electrical resistivity under elevated pressure conditions in fluid-saturated rocks (Brace et al., 1965, 1965; Daily & Lin, 1985; Han, Best, MacGregor, et al., 2011; Han, Best, Sothcott, et al., 2011; Milsch et al., 2010; Pimienta, Sarout, et al., 2017; Violay et al., 2012) and very few investigated the electrical properties—across the measuring frequency range—as a function of pressures (Jouniaux et al., 2000; Jouniaux & Pozzi, 1995). To counter this limit, we use a method known to induce a given amount of microcracks in rocks: thermal treatment (ThT), that is, applying different temperatures at slow rates on the rock sample.

Over the last decades, the ThT method has been extensively used to study the effect of slow temperature variations in different materials such as ceramics (Clarke, 1980; Davidge & Green, 1968; Evans & Clarke, 1980) or rocks (Bauer & Handin, 1983; David et al., 2001; Griffiths et al., 2018; Heap et al., 2009; Heuze, 1983; Wong, 1982a, 1982b; Wong & Brace, 1979). Different physical mechanisms were found to induce microcracks in thermally stressed materials (e.g., Davidge & Green, 1968; Fredrich & Wong, 1986), which are expected to be materials dependent. In rocks, ThT was shown to induce a homogenous and isotropic crack population if the rock was initially homogenous and isotropic (Benson, Schubnel, et al., 2006; Faoro et al., 2013; Fredrich & Wong, 1986; Nara et al., 2011; Nasseri et al., 2007, 2009; Pimienta et al., 2018; Schubnel, Benson, et al., 2006). If avoiding additional effects such as irreversible dehydration or phase transformations (Lin, 2002), applying ThT thus allows studying specifically how a crack population affects the rock effective physical properties.

In this study, bulk and pore volume, elastic wave velocities, and electrical resistivity are measured on samples before and after being submitted to different temperatures of ThT. Then, the variations in physical properties of the dry and water-saturated rocks are linked in terms of their intrinsic dependence to the evolution in microstructure using existing theories. Accounting for the frequency dependence between laboratory and field, insights from the laboratory are gained for field-scale scenario. Finally, because several rock types have been tested in the study, the effect of temperature variations on thermally induced microfracturing is discussed.

2. Materials and Methods

2.1. Rock Samples and Preparation

For the study, crustal rocks of varying mineralogical content and porosity were chosen. These are a diorite, a Carrara marble (Delle Piane et al., 2015), a Westerly granite (Fredrich & Wong, 1986), two blocks of Fontainebleau sandstone (Bourbié & Zinszner, 1985) of 4 and 6% porosity, and a Rothbach sandstone (C. David et al., 1994). All rock samples were chosen to be homogeneous and isotropic at the sample scale, although of differing mineralogical content, mineral sizes, and initial porosities.

The Westerly granite has probably been the rock the most studied in the rock mechanics community, so that its properties are well known (Faoro et al., 2013; Passelègue, Schubnel, et al., 2016; Passelègue, Spagnuolo, et al., 2016; Sondergeld & Estey, 1981; Thompson et al., 2006). Several existing studies investigated the role of ThT temperatures on some physical and mechanical properties (e.g., Fredrich & Wong, 1986; Griffiths et al., 2017; Nasseri et al., 2007, 2009; Wang et al., 2013). Similar to most granites, the rock is made of crystals of quartz (approximately 27%), feldspars, biotites, and other constituents. The minerals are randomly distributed so that the rock is usually considered isotropic at the sample scale, and the average grain size is about 500 μm (Fredrich & Wong, 1986).

The Carrara marble has also been largely used in the rock mechanics community (Delle Piane et al., 2015; Ramez & Murrell, 1964; Sarout et al., 2017; Schubnel et al., 2005; Schubnel, Walker, et al., 2006). It is a 99% calcite marble, constituted of randomly oriented well-sorted calcite crystals with an average grain size

of about 150 μm (Delle Piane et al., 2015). Often, the rock is considered to be of very low porosity, with properties very near the ones of calcite. Moreover, existing work reports investigations of thermal quenching on rock samples (Delle Piane et al., 2015; Sarout et al., 2017), from a sudden immersion of a hot sample (i.e., 300 or 600 °C) in cold water.

The Fontainebleau sandstone originates from two distinct blocks from Fontainebleau quarry. It is a well-known rock in the rock mechanical and physics community (Bourbie & Zinszner, 1985; Gomez et al., 2010; Pimienta, Fortin et al., 2014; Pimienta et al., 2015a; Song & Renner, 2008). The rock is clean (i.e., approximately 100% quartz), made up of quartz grains of about 200 μm cemented by a quartz matrix (Song & Renner, 2008). The grains are well sorted and randomly oriented, generally making for a rock homogeneous and isotropic at the sample scale (Pimienta et al., 2015a, 2015b). An additional interest of this rock is that it spans a large porosity range, from 3% to about 25%, which usually depends on the rock degree of cementing (Bourbie & Zinszner, 1985; Pimienta, Fortin et al., 2014). As a direct consequence, permeability spans several orders of magnitude (Bourbie & Zinszner, 1985) and a large range in *P* and *S* wave velocity is covered across the porosity range (Gomez et al., 2010; Pimienta, Fortin et al., 2014).

The Rothbach sandstone is a reddish rock originating from the Vosgian sandstone formation (David et al., 1994; Louis et al., 2007, 2009). Its modal composition is about 70% quartz, 16% feldspars, and 12% clays (David et al., 1994). Its reported porosity is usually about 20% (David et al., 1994; Louis et al., 2007, 2009). The larger average porosity of about 25% measured in all initial/nontreated samples of this study might link to the formation layer with coarser grains (Louis et al., 2009), of about 250 μm. The rock is slightly layered, so that *P* wave velocities were shown to be anisotropic, by about 5% (Louis et al., 2009). In this study, two samples—cored either perpendicular or parallel to bedding—were submitted each temperature of ThT.

The diorite chosen originates from a quarry in the U.S., which exact location could unfortunately not be determined. The rock is, however, used as being very stiff and with no preexisting cracks; that is, the porosity of intact samples is in the measurement error of 0%. Similarly to the uncracked Frederick diabase (Brace, 1965b; Fredrich & Wong, 1986), this will allow a perfect investigation of the effects of thermally induced microcracks on the physical properties. Its grains are approximate of a millimeter size. The sample composition determined from X-Ray Diffraction (XRD) analysis is ~57% plagioclase-Na, ~27% feldspath-K, ~8% quartz, and ~7% mica. Samples proved to be homogeneous and isotropic at the sample scale, constituted of well-sorted and randomly oriented grains.

Samples of all rocks were prepared as cylinders of about 38-mm diameter and 20-mm length. For each rock, about 10 samples have been prepared, each one to be subjected to a given target temperature of ThT. ThT is applied in an oven that allowed for temperatures up to 1,000 °C. The ramp of temperature increase is chosen to be 5 °C/min (Figure 1), which is expected to allow for homogeneous temperature increase across the sample lengths (i.e., 20 mm) and radius (Wang et al., 2013). Once reaching the target value, temperature is maintained during 1 hr and then the hoven is switched off so that temperature decreases overnight with a ramp slower than 1 °C/min.

2.2. Measuring Protocol

Porosity variations intrinsically relate to variations in the sample pore and/or bulk volume, which could be caused by different effects such as mineral transformation or creation of a new porosity. Under the understanding that samples outer (i.e., bulk) and inner (i.e., pore) volumes may not evolve in the same manner, the volume variations were tracked with two distinct methods. Bulk volume variations were attained from the variations in sample length (L) and diameter (2R), so that $\Delta V = \Delta L + 2\,\Delta R$. Those lengths were measured with an electronic caliper accurate to about 1 μm, leading to measured variations of $\Delta L = L_f - L_i$ and $\Delta R = R_f - R_i$. Pore volume variations ($\Delta\phi$) were attained from measuring the pore volume before and after ThT, using a pycnometer with an accuracy of 10^{-3} cm^3. These were double-checked by measuring the mass variation between dry and water-saturated samples, using a balance with an accuracy of 1 mg.

Ultrasonic *P* and *S* wave velocities were acquired at high frequency ($f = 1$ MHz) from applying a pair of either *P* or *S* piezoelectric PI transducers across the sample length. *P* and *S* wave velocities were then obtained from manually peaking the first arrival of the wave across the sample length. The velocities were measured on samples both dry and water fully saturated. Electrical impedance across the sample length was recorded with a *Solartron* electrical impedance apparatus, allowing measurements over a frequency band of 10

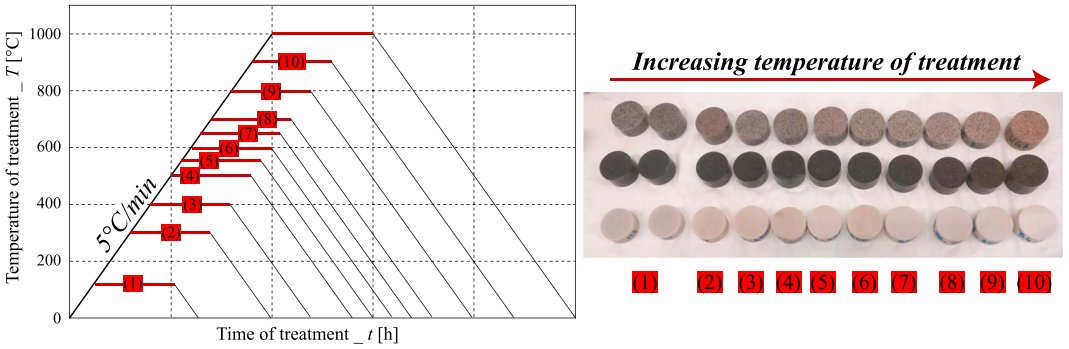

Figure 1. Protocol of thermal stressing of the rock samples. Temperature is increased at a rate of 5 °C/min up to a target temperature then kept constant during one hour. Then, the oven stops and temperature slowly decreases, overnight, at a rate below 1 °C/min.

mHz to 1 MHz, using a two-electrode setup with one guarding electrode to minimize the lateral surface effects. Electrodes were in brass, and measurements were made by applying alternative current with voltage excitations of 10 mV. The apparatus is rated to perform precise measurements in the range of 1 mΩ to 1 MΩ on small samples, with lengths below 25 mm.

The acquired electrical impedance is recorded as a complex signal $\overline{Z} = |Z|e^{i\phi}$, composed of an amplitude $|Z|$ and a phase ϕ. Measurement was made over 31 logarithmically distributed frequencies in from 100 kHz to 0.1 Hz. Samples were measured under dry and brine-saturated conditions. Three rocks of FoS6, Westerly granite, and diorite were measured with seven saturating brines of varying salinity, spanning conductivities from 450 μS/cm (distilled water) up to about 29.1 mS/cm for a distilled water saturated by dissolved NaCl ions. Noting that most surface effects were not observed for brines salinity above 1 mS/cm for the three rocks, a brine conductivity of $\sigma_w = 3.2$ mS/cm was chosen for measurements of all rocks. Because phase was at its lowest for this frequency, electrical resistance measurement was attained at 10 kHz. The sample intrinsic resistance $|Z| \sim Z_s$ was used to determine electrical resistivity $R_s = Z_s{}^S/_L$ across the sample length L and area S. The formation factor $F = \sigma_w R_s$ was finally inferred to compensate for the effect of the brine conductivity.

For the three samples tested at very different brine conductivities, results under saturation by the high-salinity fluid are also reported and qualitatively investigated. Although polarization at the electrodes might occur at frequencies below 1 kHz in a two-current electrodes setup (Revil et al., 2014), our measurements relied on alternative current excitations of very small voltages (i.e., of 10 mV), so that the low-frequency data set will still be qualitatively investigated in the following.

3. Experimental Results

The rock sample porosities were measured, as well as their *P* and *S* wave velocities and electrical resistivities under dry and water-saturated conditions (Table 1). For all rocks, the electrical resistivity of the dry samples after any ThT temperature is about 1 MΩ; that is, none of the rocks chosen bears an initial conductive matrix, so that all can be considered as insulating materials in which the conductivity occurs only from the presence of fluids. From its larger porosity and lower ultrasonic wave velocities and formation factor, the porous Rothbach sandstone has a distinct behavior. Except for this rock, the porosities of the untreated rocks range from 0.1 to 6%, and *P* wave velocities of the dry samples range from 4.2 to 6.3 km/s. Under brine-saturated conditions, *P* wave velocities range from 5.1 to 6.4 km/s. Under brine saturation, the diorite and marble samples exhibit very high electrical resistivity (i.e., formation factor above 8,000). The sandstones show lower electrical resistivity, which originates from bulk hydraulic conduction through a naturally existing porous network. Despite its low porosity, the untreated Westerly granite sample also shows a lower electrical resistivity and relatively low *P* and *S* wave velocity values compared to those found in the literature at high confining pressure (Wang et al., 2013), which could be explained by a preexisting crack network inside the rock sample. A range of variability is obtained for the formation factor measured on different intact samples, which is not small in diorite and FoS6 samples. For the diorite, variability might link to the presence of

Table 1
Average Grain Size Estimated From Scanning Electron Microscopy and Literature (Bourbié & Zinszner, 1985; Delle Piane et al., 2015; Fredrich & Wong, 1986; Insun Song & Renner, 2006) and Measured Physical Properties of the Intact Rock Samples Under Dry (Porosity, V_p, and V_s) and Water-Saturated Conditions (V_p and V_s)

	Quartz content	Grain size	Porosity (%)	Vp (dry; km/s)	Vs (dry; km/s)	Vp (sat; km/s)	Vs (sat; km/s)	FF (sat)
Carrara Marble (CarMbl)	0%	200 μm	0.1	6.21	3.32	6.41	3.29	6415–6335
Diorite (Dior)	30%	> 1 mm	0.1	6.29	3.46	6.43	3.53	8687–19205
Westerly Granite (WGs)	25%	500 μm	0.8	4.19	2.73	5.46	2.96	1800–2147
Fontainebleau (FoS4)	100%	200 μm	3.6 (±0.4)	5.28	3.40	5.12	3.09	1534–1951
Fontainebleau (FoS6)	100%	200 μm	6.1 (±0.4)	5.21	3.52	5.18	3.24	475–2085
Rothbach sandstone (RothS)	70%	250 μm	25.9 (±0.7)	2.91	2.00	3.57	2.88	22–23

Note. A range in initial formation factor is measured under brine-saturated conditions from the variability in the intact samples.

a very thin conductive network in some samples (i.e., FF = 9,000) and not in the others, with such lower values still remaining the highest found in the intact samples. For FoS6, this variability links to the slightly larger pore size for the sample of lower FF = 500. In the following, we investigate the evolution in the rocks physical properties with varying ThT.

3.1. Microstructure and Volumes Variations

To ascertain the intrinsic effect of ThT, samples of each rock either untreated and after a chosen temperature of ThT were imaged (Figure 2) using Scanning Electron Microscopy. All samples submitted to a large temperature of ThT exhibit microcracks (Figure 2), which are mostly intergranular. In the particular case of Carrara marble, spherical micropores could also be observed in few locations.

Measuring bulk (Figure 3a) and pore (Figure 3b) volume variations from heating at different temperatures highlight an evolution in the rock microstructures that differs from one rock to the other. For all rocks except Rothbach sandstone, very similar increases are observed between bulk and pore volume variations. It implies that the increase in the bulk, outer, volume solely originates from the pore volume one. A new porosity is created that leads to irreversible expansion of the rock sample, and no irreversible mineral transformation occurs. For the Carrara marble, spherical micropores are observed (Figure 2) but do not appear to affect the measured overall porosity (Figure 3b) because their concentration might be low. For Rothbach sandstone, the deviations link to the much lower accuracy of measurement of small porosity variations in very porous media.

3.2. Ultrasonic Wave Velocities

An overall decrease is observed from the measured *P* and *S* wave velocities of the dry (Figures 4a and 4b) and water-saturated (Figures 4c and 4d) samples. Under dry conditions, except for Rothbach sandstone (i.e., 30% decrease), all samples show a dramatic decrease to about 30–40% of the rock initial value (i.e., 70% decrease) at maximum ThT. This decrease is similarly large for both *P* and *S* wave velocities but smaller under water-saturated conditions. Consistent with the volume variations, the ThT temperature for the decrease differs between the Carrara marble and the other rock samples. For all rocks except Carrara marble, the decrease in velocities starts at a temperature of 400 °C and reaches its minimum at 600 °C. For the Carrara marble, a large decrease is already observed as temperature reaches 200 °C and the asymptote is reached at 400 °C.

3.3. Electrical Resistivity and Formation Factor

3.3.1. Bulk Resistivity and Formation Factor

Under brine-saturated conditions, large decreases in formation factor *F* are observed as a function of ThT for all rocks (Figure 5), which can be as large as 2 orders of magnitude. As for the volumes and velocities (Figures 3 and 4), sandstones show less change with ThT than the low-porosity crustal rocks. Similarly to its other physical properties, the decrease in formation factor starts at 400 °C and reaches its constant minimum value starting from 600 °C for most rocks except for the marble. In case of the marble, a strong decrease was observed from temperatures of 200 °C.

3.3.2. Electrical Impedance and Phase Peaks

Investigating the frequency-dependent electrical impedance highlights a phase peak in the low-frequency range, in the range of 1–10 Hz. This phase peak depends on both the brine electrical conductivity and the degree of ThT the sample was subjected to. For the example of three rock samples (FoS6, Diorite, and

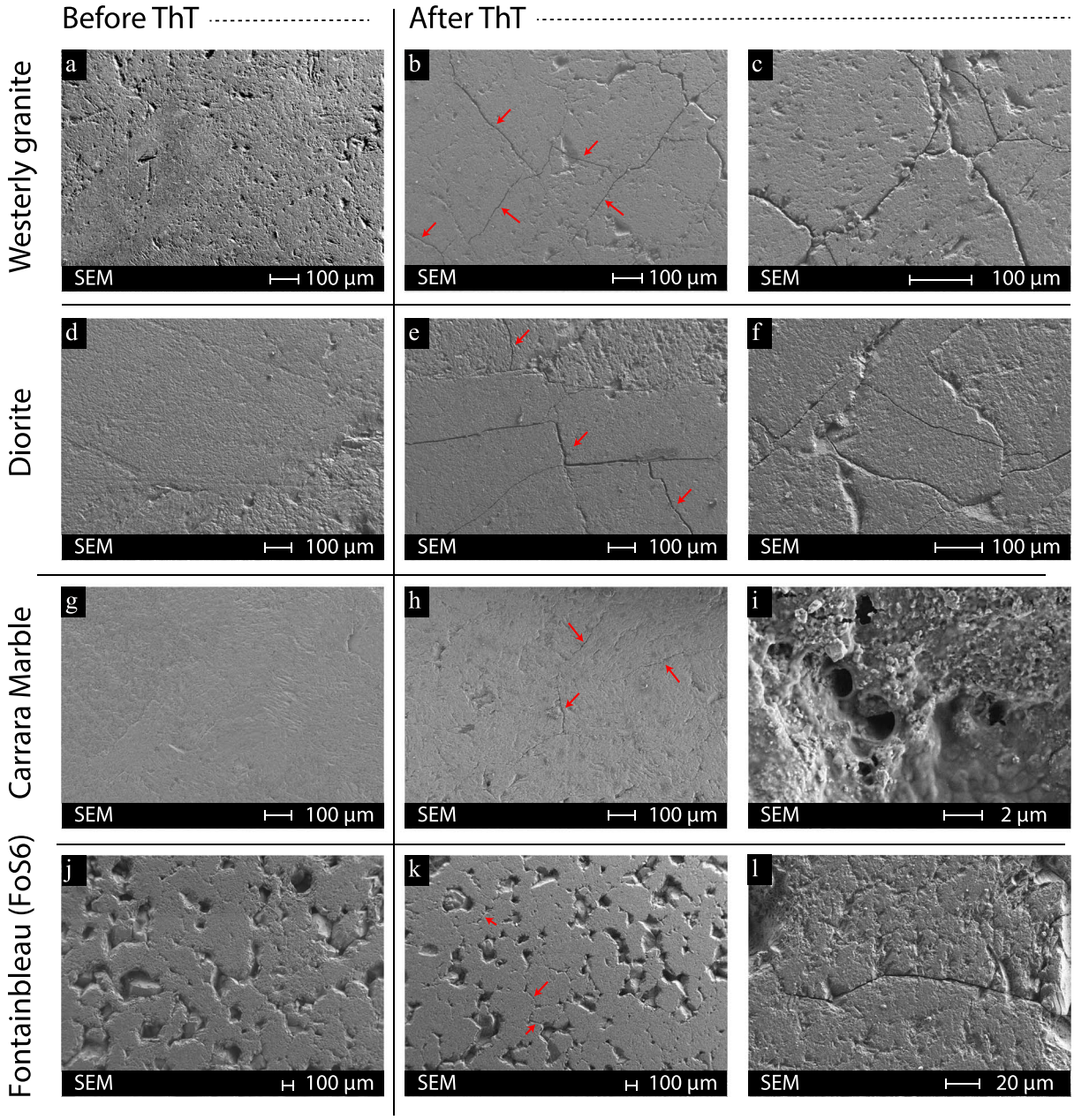

Figure 2. Scanning Electron Microscopy observations of the polished surfaces of the rock samples nontreated and after ThT for four rock samples of (a, b, and c) Westerly granite; (d, e, and f) Diorite; (g, h, and i) Carrara marble; and (j, k, l) 6% porosity Fontainebleau sandstone (FoS6).

Granite) saturated by the brine of 29.1 mS/cm electrical conductivity, the impedance phase is reported as a function of frequency (Figures 6a–6c). Most samples highlight a phase peak at a frequency of about 10 Hz, which appears to increase in magnitude, and slightly shift to higher frequency, as the temperature of ThT increases. Interestingly, while the samples of granite and FoS6 before ThT have an initial phase peak of about 100–150 mrad (Figures 6a and 6b), the intact diorite samples do not exhibit any peak (Figure 6c).

Characterizing the variations (Figures 6d–6f), the phase changes reach very large magnitudes of up to about 400 mrad beyond 600 °C for all three rocks (Figure 6e). The variation is also linked to an increase in frequency of the peak, from about 4 Hz to about 8 Hz (Figure 6d). Normalizing the change in magnitude (Figure 6f), about the same variations are observed for the granite and diorite samples, which is twice greater than the Fontainebleau sandstone. Interestingly, those temperature-dependent evolutions correlate directly to the evolution in volumes of those rock samples (Figure 3).

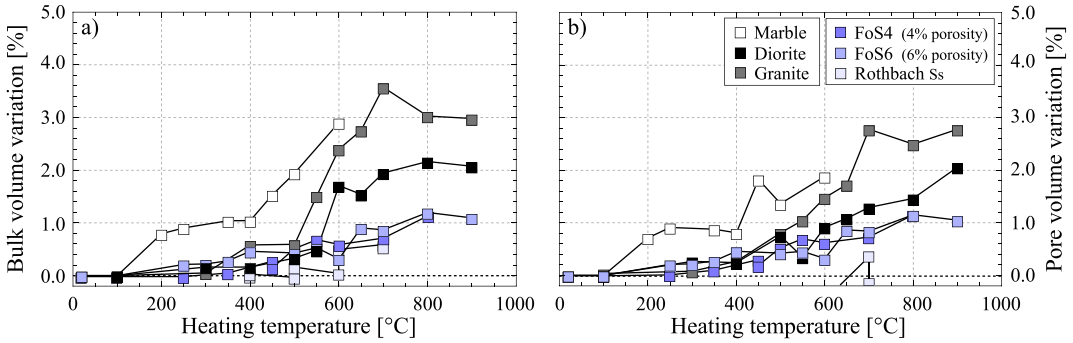

Figure 3. Measured (a) bulk and (b) pore volume variations for the rock samples as a function of the temperature of thermal treatment (ThT).

4. Interpretations

4.1. Relative Effect of Cracks on the Effective Properties

4.1.1. Elastic and Electrical Properties Versus Porosity

P wave velocity of the dry and water-saturated samples is compared to the measured porosity (Figure 7a). Although with very small porosity variations, samples exhibit dramatic drops in *P* wave velocity in the low-porosity rocks, which is consistent with the effects of cracks on rocks elastic properties (Guéguen et al., 2009; Walsh, 1965b). Although of initial values as high as 6 km/s, the *P* wave velocity for most low-porosity rocks decrease down to values lower than any of the Rothbach sandstone samples. The high temperatures of ThT have a much stronger effect on the low-porosity rocks than on the high-porosity ones. Once the samples are water saturated, consistent with theories in microcracked media (Adelinet et al., 2011; Kachanov, 1993; Pimienta et al., 2015a; Wang et al., 2012), ultrasonic *P* wave velocity increases by about 2 km/s for most rocks.

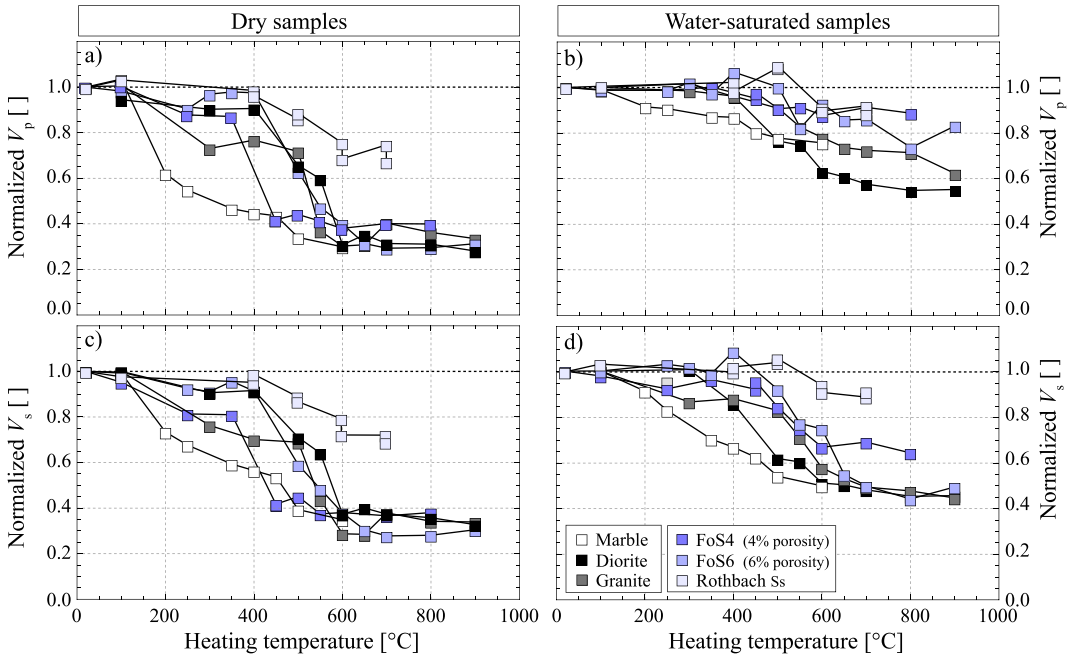

Figure 4. Measured (a, b) *P* and (c, d) *S* wave velocities variations for the dry and water-saturated rock samples for the different degrees of ThTs. The variations in properties are obtained from normalizing the wave velocities with measurements at lowest temperature, not thermally treated.

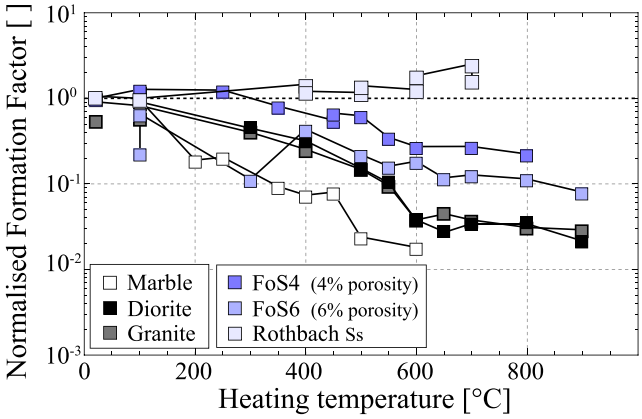

Figure 5. Normalized electrical formation factor F for the different rocks as a function of the temperature ThT, from measured electrical impedance at a frequency of 10 kHz on the rocks saturated by a brine with an electrical conductivity of about 3.2 mS/cm.

Further comparing formation factor-to-porosity (i.e., F-ϕ) variations with that reported in the literature (Figure 7b). Usual F-ϕ data sets aiming at the linking of the properties from varying one single parameter (e.g., pore size) investigate natural rocks that span porosities from 5% to about 30% (Lesmes & Friedman, 2005; Lesmes & Frye, 2001; Pimienta, Sarout, et al., 2017; Revil et al., 2014, 2015; Titov et al., 2010; Tong et al., 2006; Weller et al., 2011). This new data set investigates specifically the effects of microcracks and evidences a change of slope in the F-ϕ trend for porosities below 5–7%, when compared to usual trends. Below 5% porosity, very small porosity variations might induce extreme variations in F, from about 10^4 to 10^2. Consistent with measured properties as a function of confining pressure (Pimienta, Sarout, et al., 2017), and with permeability-porosity trends in some rocks (Bourbie & Zinszner, 1985), interconnected crack networks might strongly affect the electrical formation factor although not affecting much the overall porosity. Moreover, almost no effect is observed in very porous rocks although crack porosity had increased (Figures 3a and 4), which is consistent with earlier observations (Pimienta, Sarout, et al., 2017).

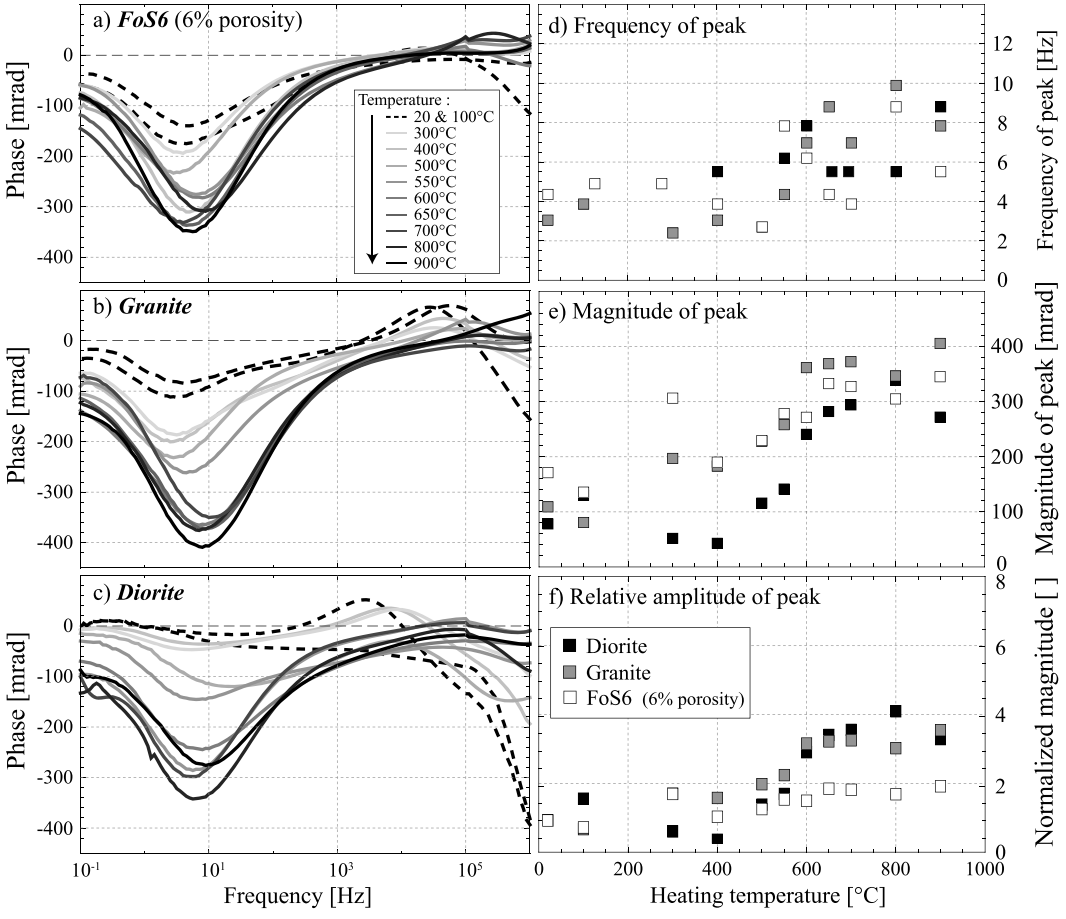

Figure 6. Measured phase of electrical impedance as a function of the frequency for (a) the 6% porosity Fontainebleau sandstone, (b) the granite, and (c) the diorite, for a brine electrical conductivity of 29.1 mS/cm. The evolution with the temperature is highlighted as evolution in grey level, from the treatment at 300 °C (light gray) to the one at 900 °C (black). The peak in phase observed at low frequency is automatically peaked to get the (d) frequency, (e) amplitude, and (f) relative variations of peak amplitude.

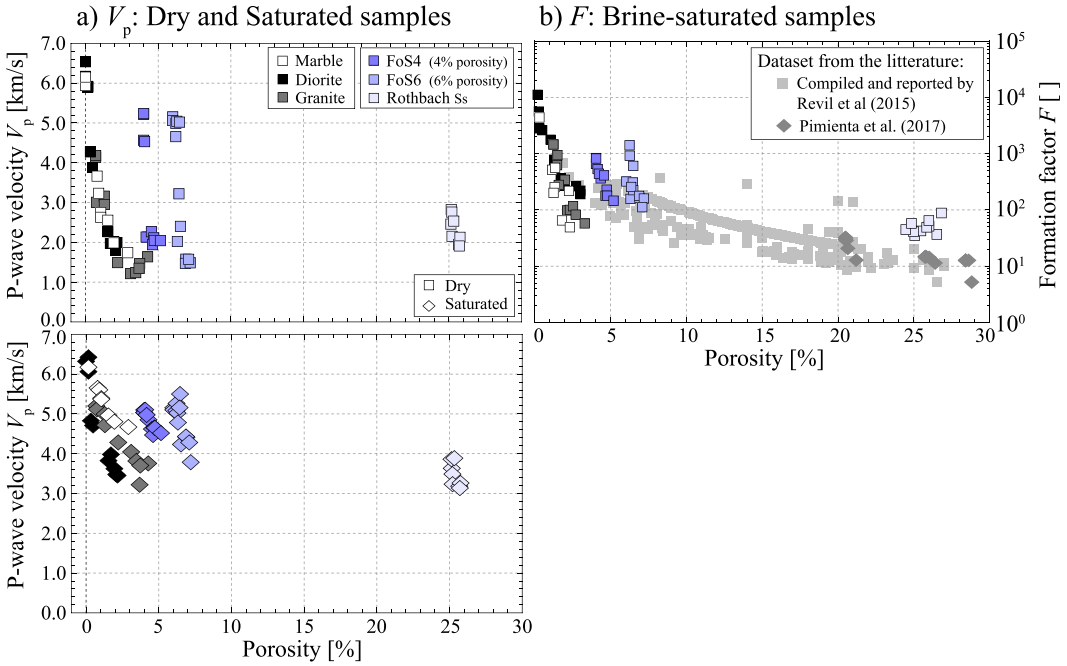

Figure 7. Measured (a) *P* wave velocity of samples, either dry (i.e., squares) or water saturated (i.e., diamonds), as a function of the porosity, and (b) *F* of the brine-saturated samples (i.e., $\sigma_w = 3.2$ mS/cm) as a function of the porosity, compared to F-ϕ trends for various rocks at ambient pressure (Lesmes & Friedman, 2005; Lesmes & Frye, 2001; Revil et al., 2014, 2015; Titov et al., 2010; Tong et al., 2006; Weller et al., 2011), and a study of the pressure-dependent F-ϕ trends for three rocks (Pimienta, Sarout, et al., 2017), found in the literature.

Although porosity variations are small, dramatic decrease in *P* wave velocity and formation factor are evidenced. These link to the creation of a family of thin elongated microcracks (Guéguen & Kachanov, 2011; Kachanov, 1993; Walsh, 1965b, 1965bc), which is consistent with theories of ThT effects in rocks (Fredrich & Wong, 1986). The existence of this family of cracks is further confirmed by the large increase in the samples' *P* and *S* wave velocities from dry to water-saturated conditions (Figure 7a). This variation highlights the stiffening effect of water on the wave velocities at the ultrasonic frequency of measurement (Fortin et al., 2014), which is expected to occur predominantly when thin elongated cracks are present (Adelinet et al., 2011; Fortin et al., 2014; Guéguen & Kachanov, 2011; Gurevich & Makarynska, 2012). Because properties in Rothbach sandstone are dominated by the pore network, the rock is not used further to investigate the specific effects of varying crack densities on the effective properties.

4.1.2. Microcrack Density and Aspect Ratio

To investigate further the created microcracks, effective medium theories can be used (Guéguen & Kachanov, 2011; Kachanov, 1993). Following many earlier approaches (Faoro et al., 2013; Pimienta, Sarout, et al., 2014; Wang et al., 2013), we assume here that the created porosity ϕ_c is made of thin elongated spheroidal cracks ($\phi_c = \frac{4}{3}\pi\xi\rho$), represented by a mean aspect ratio ξ (i.e., opening over length, $\xi = w/l$) and a crack density (Guéguen & Kachanov, 2011; Kachanov, 1993):

$$\rho = \frac{1}{V}\sum_{k=0}^{n} l_k^3, \tag{1}$$

where l_k is the length of the *k*th microcrack and *n* is the amount of microcracks contained in the representative elementary volume *V*. To model the effects of a distribution of cracks on the effective elasticity of an isotropic medium, we use the same modeling as that in Pimienta et al. (2018), also detailed in Appendix A. To characterize the effects of ThT, the microcrack density (ρ) is inverted from minimizing the least squares difference between model and measurements (e.g., Pimienta, Sarout, et al., 2014).

Consistent with the measured *P* wave velocity drop, large increase in crack density is observed as the temperature of ThT increases, reaching similar values for all rocks (Figure 8a). Again, a differentiation is

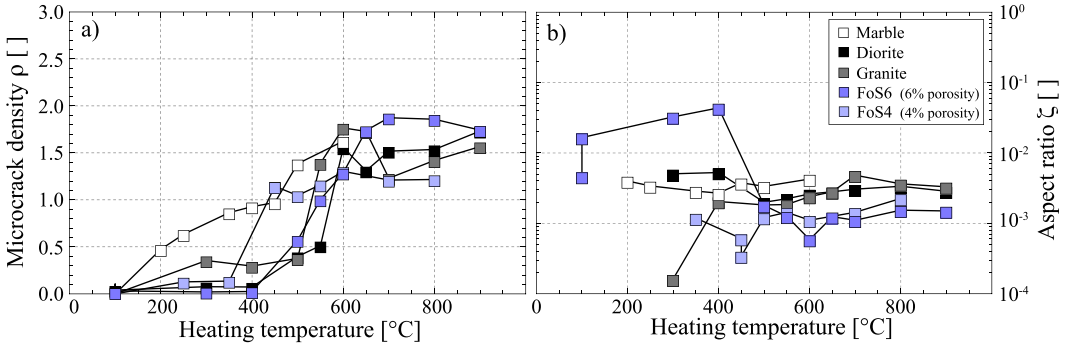

Figure 8. For the different rocks, dependence to temperature of ThT of (a) inverted apparent microcrack density ρ, from least squares inversion between measured and modeled *P* wave velocity, and (b) calculated aspect ratio ζ, from combining microcracks density ρ and crack porosity ϕ_c.

observed between rock samples. For all the rocks, the inferred ρ is as high as about 1.5 at temperatures beyond 600 °C. However, it is still used as being the one found to allow for lowest errors. The aspect ratio (ξ) is calculated from the inverted ρ and the measured porosity variation (Figure 8b), using the equation of the crack porosity $\phi_c = \Delta V = \frac{4}{3}\pi\xi\rho$. No clear variation in aspect ratio with varying ThT is observed (Figure 8b), with an average value of $\xi = 1\text{–}5 \cdot 10^{-3}$ for all samples. Hence, the method does not appear to efficiently highlight the evolution in cracks opening often observed by optical studies (Fredrich & Wong, 1986; Nasseri et al., 2007) and also possibly inferred from the shift in frequency of the electrical impedance phase peak (Figure 6).

4.1.3. Inferred Permeability

Permeability links directly to the rock porous network, in terms of its concentration and its connectivity (Bernabé, 1991; C. David et al., 1993, 2018; Guéguen & Dienes, 1989; Pimienta, Sarout, et al., 2017; Sarout, 2012). Assuming simple geometries of either tubes (i.e., connected spherical pores) or penny-shaped cracks, one could predict the permeability of a material. In the particular case of a purely microcracked rock with penny-shaped isotropic cracks, one gets (Benson, Meredith, et al., 2006; Guéguen & Dienes, 1989)

$$\kappa_c = \frac{2}{15} f_c w^2 \xi \rho, \tag{2}$$

where w is the crack aperture and ρ and ξ are the crack density and aspect ratio. The percolation factor f_c describes the connectivity of the crack network (Guéguen & Dienes, 1989) and can be approximated as $f_c = \frac{9}{4}\left(\frac{\pi^2}{4}\rho - \frac{1}{3}\right)^2$. Moreover, using the same models, a link exists between formation factor and porosity—hence between permeability κ and formation factor F—such that (Guéguen & Dienes, 1989; Pimienta, Sarout, et al., 2017)

$$\kappa_F = \frac{8}{15} F^{-1} w^2, \tag{3}$$

Consistent with earlier discussions, this model implies that the product between permeability and formation factor is proportional to a length scale squared (Sun & Wong, 2018; Walsh & Brace, 1984). Interestingly, no percolation threshold is needed once the formation factor F is known. From the existing models, both F and κ are expected to intrinsically depend on the connectivity between microcracks in a very similar manner (Guéguen & Dienes, 1989). The two models can thus be applied separately—on either elastic microstructural variables (i.e., κ_c, equation (1)) or formation factor (i.e., κ_F, equation (3))—to compare the evolution in inferred permeability with varying temperatures (Figure 9).

To investigate how the microcrack network affects the inferred permeability, predictions of κ_c with either a constant $f_c = 1$ (i.e., κ_1, Figure 8a) or a variable $f_c = f(\rho)$ (i.e., κ_2, Figure 9b) are plotted for the different samples as a function of κ_F. For the predictions, the measurements used start at 200–250 °C, once crack density is not zero. The remaining unknown for all predictions, the cracks opening, is chosen constant to $w = 1$ μm. Surprisingly, while κ_1 fits tightly with κ_F, it is not the case of κ_2. Although κ_F is always slightly larger than

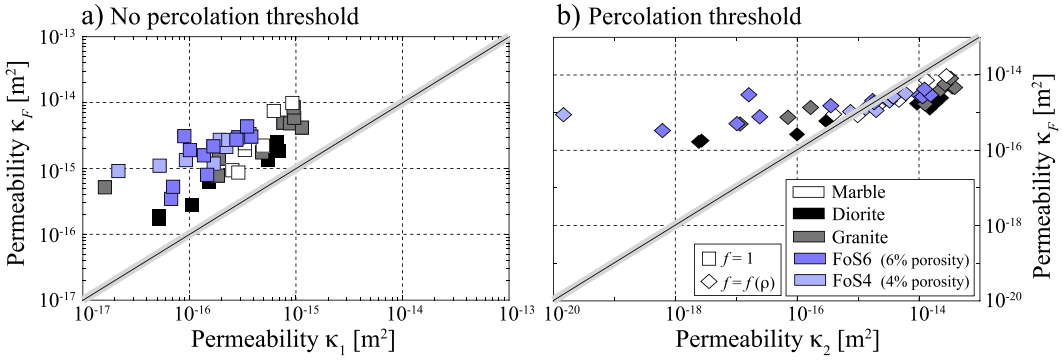

Figure 9. Comparison between inferred permeability values for the different rock samples using either elastic (i.e., κ_1) or electrical (i.e., κ_2) properties, assuming a crack mean opening of 1 μm for all predictions. Permeability inferred from formation factor κ_F as a function of (a) the crack permeability κ_1 assuming cracks always connected (i.e., $f = 1$); (b) the crack permeability κ_2 using the percolation $f_c = f(\rho)$ function (Guéguen & Dienes, 1989).

κ_1, the two exhibit variations of up to about 2 orders of magnitude in some samples. Reversely, κ_2 predicts variations of up to 4 orders of magnitude.

Note in particular the very high permeability values at lowest crack densities, larger than about $\kappa = 10^{-17} - 10^{-16}$ m^2, even though measurements are at ambient pressure. In the porous rocks, this behavior is consistent with the existence of a pore network in parallel of the crack one (Bernabé, 1991; David et al., 1993; Guéguen & Dienes, 1989). In purely microcracked rocks, however, typical measurements are of $10^{-19} - 10^{-18}$ m^2 (Brace et al., 1968; David et al., 2018; Faoro et al., 2013) or below as confining pressure closes the microcracks. This points out to whether F and κ could be compared in low-porosity/permeability rocks with low crack densities. In the particular case of the nonporous marble and diorite, κ should tend toward zero if no cracks are present. Two possible causes are that (i) the chosen w values might overestimate the real ones, which would increase the effect of F variations over that of κ, or (ii) an intrinsic difference exists between the two properties.

Because one expects cracks maximum length to be of the grain size, w might not be much smaller than $w =$ 0.1–1 μm, consistent with values reported in the literature (Benson, Meredith, et al., 2006; Wang et al., 2013). Second, comparing hydraulic and electrical conductivities relies on the assumption that the rock matrix is nonconductive so that both molecules and currents are solely transmitted through the cracks/pores networks. While this is exact for hydraulic conductivity, it remains an approximation for electric conductivity. Dry rocks have electrical resistance of about 1 MΩ, that is, only one order of magnitude larger than the measured value under brine-saturated conditions in the loosely cracked rocks.

4.2. Frequency Dependence and Insights for Field Scale

When aiming at comparing the two properties in the laboratory, it is of interest to attempt extending to field scales. For the two properties, a parameter to account for is the frequency at which the measurements are made. In the laboratory, both elastic wave velocities (approximately 1 MHz) and electrical resistivity (approximately 1–10 kHz) are attained in the high-frequency range. However, the two properties are obtained on the field at a much lower frequency of about 1–10 Hz or below, and both elastic (e.g., Fortin et al., 2014; Müller et al., 2010; Pimienta et al., 2016) and electrical (Clennell, 2010; T. Han et al., 2015; Jouniaux et al., 2009; Jouniaux & Pozzi, 1995; Maineult et al., 2018; Revil et al., 2015) properties are frequency dependent. It is thus of interest to investigate the effects of cracks on the two properties one could expect at much lower frequencies.

4.2.1. Electrical Impedance at Low Frequencies

Very large increases in phase shifts have been observed (Figures 6a–6c) in the studied rocks with increasing the degree of microfracturation (Figures 8). Although the electrodes polarization effects could be in cause (Tirado et al., 2000), we expect it not to occur here from the low voltage of the measurements. It is thus of interest to investigate the evolution in phase shifts for the *same* rock samples—but increasing degree of microfracturation—saturated by the same pore fluid. For instance, almost no phase shifts were observed

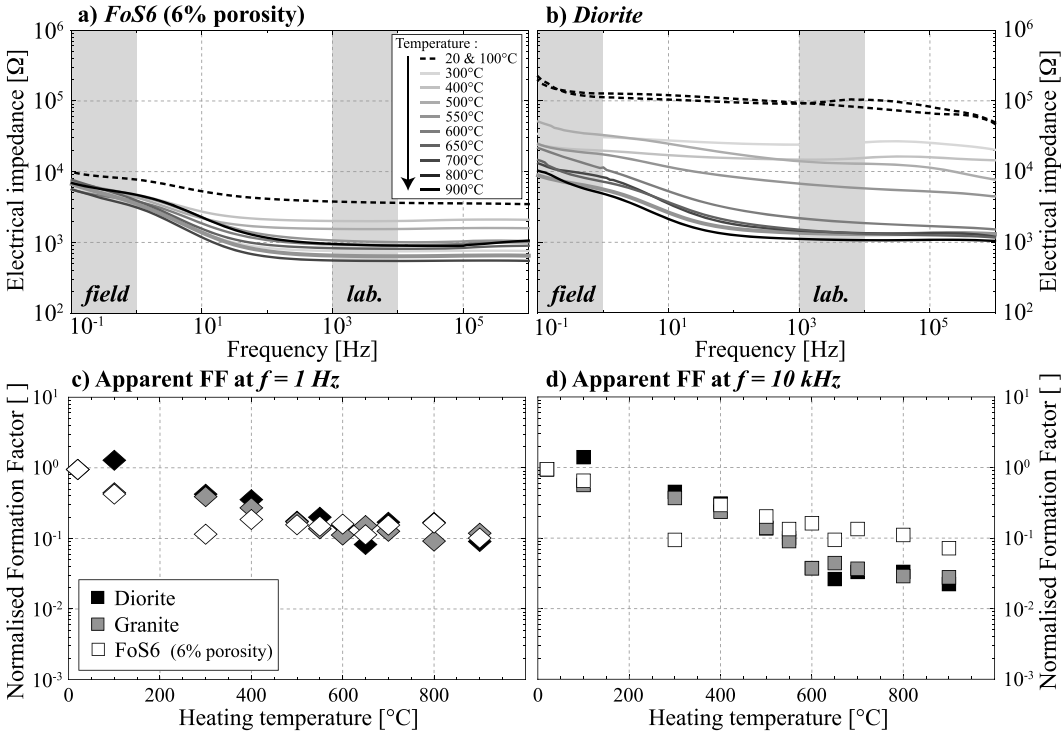

Figure 10. Example of measured frequency-dependent amplitude of the electrical impedance (corresponding to the phase in Figure 6) for (a) the 6% porosity Fontainebleau sandstone (Fo6) and (b) the diorite. Inferred apparent formation factor from measured impedance amplitude, with NaCl brines with an electrical conductivity of 29.1 mS/cm, for frequencies of (c) 1 Hz and (d) 10 kHz.

in the *intact* crack-free diorite samples (Figure 6c). For this rock, the increase in increasing crack porosity (Figure 3) directly correlates with the phase shift frequency (Figure 6d) and amplitude (Figures 6e and 6f). For the initially porous sandstone (Figure 6a) and microcracked granite (Figure 6b), the same increase in phase shift frequency (Figure 6d) and relative amplitude (Figure 6f) is observed, although starting from a nonnull phase shift as the rock initially had pores.

Two effects are evidenced from the variations in the characteristic frequency and magnitude of the peak. Investigating the underlying physics (Maineult et al., 2018; Revil et al., 2012, 2015; Tong et al., 2006), these are consistent with the thermally induced crack porosity increases (Figure 3) that are expected to contain informations in both pore size and amount of pores (Guéguen & Palciauskas, 1994; Walsh, 1965b). The magnitude increase of the peak phase with ThT (Figure 6f) directly correlates with the porosity variations (Figure 3), and not with the inverted microcracks density (Figure 8a) that reaches the same maximum value for all samples. The variations of the phase peak frequency link to a characteristic relaxation time τ_0 that can be defined such that (Revil et al., 2012)

$$\tau_0 = \frac{\Lambda^2}{2D_{(+)}}, \tag{4}$$

where Λ is the characteristic pore size leading to the effect and $D_{(+)}$ is the diffusion coefficient in the Stern layer (Revil et al., 2015). Assuming $D_{(+)}$ to be constant with the temperatures of ThT, the evolution in τ_0 (i.e., frequency) thus directly highlights a variation in the cracks opening. The characteristic size is here expected to be the cracks aperture w. Because the average variation with temperature is from 4 to 8 Hz for all three rock samples (Figure 6), it implies that w should indeed increase with the target temperature of ThT for all three rocks. The reason for an absence of increase in cracks aspect ratio ξ (Figure 7b) might be that the crack length l also increases at the same time as w.

At this point, it is of interest to note that intense dispersion phenomena could occur in microcracked rocks (Figures 10a and 10b): The frequency-dependent increase in electrical impedance amplitude directly

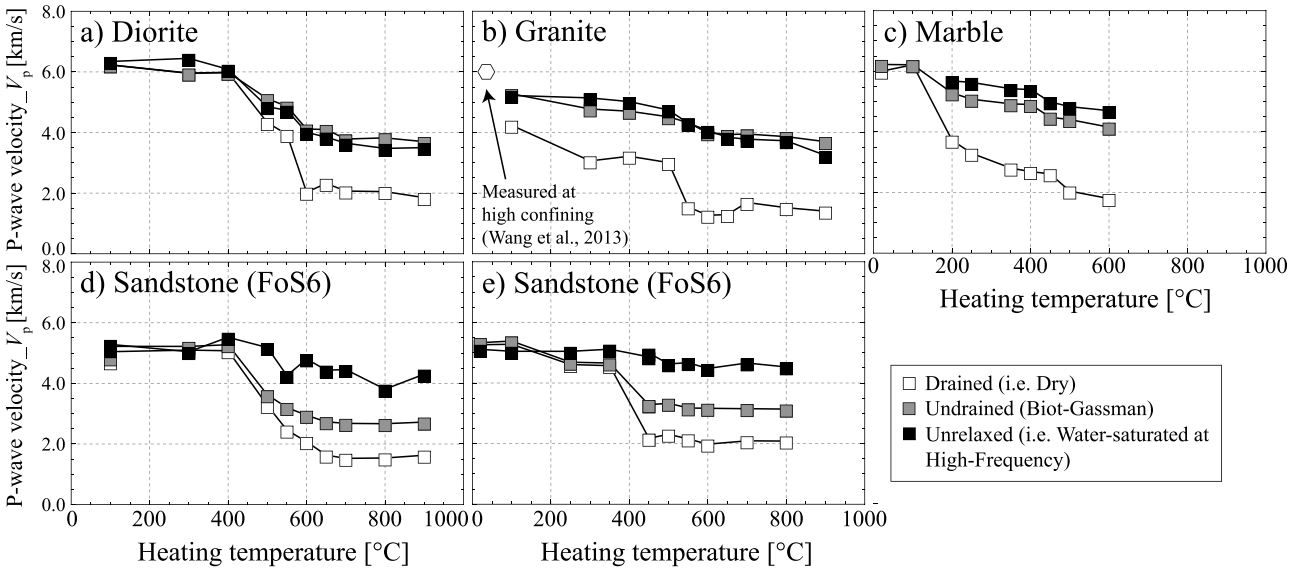

Figure 11. Comparison *P* wave velocity of the (a–e) different rock samples between the (i) measured drained (or dry) regime, (ii) inferred undrained regime, and (iii) measured water-saturated high-frequency regime.

increases with the degree of microfracturing of the rock sample. In other words, the difference between intact and cracked rocks at 1 Hz (Figure 10c) has decreased by about 1 order of magnitude as compared to that measured at 10 kHz (Figure 10d). For the example of the three rocks studied, the drop in apparent formation factor at 1 Hz is of about 1 order of magnitude for all three rocks. It implies that while clearly observable at the laboratory scale, the effect of microfracturing might be less noticeable at the field scale.

4.2.2. Elasticity at Low Frequency: Effect of the Porous Network

Recent laboratory measurements across the frequency range reported elastic dispersions beyond 100% in fluid-saturated natural sandstone samples with an initial large microcrack network (Pimienta et al., 2016; Pimienta, Borgomano, et al., 2017). These frequency-dependent dispersions originate from fluid flow at different scales (Fortin et al., 2014; Gurevich et al., 2010; Le Ravalec & Guéguen, 1996; Müller et al., 2010; O'Connell & Budiansky, 1977; Rice & Cleary, 1976), which needs to be accounted for when aiming to link laboratory and field measurements (Mavko et al., 2003).

Although, in this study, *P* and *S* wave velocity could not be measured here as a function of frequency, it is possible to assess the properties for the three elastic regimes (Adelinet et al., 2011; Fortin et al., 2014) expected in the relevant frequency range. From the ultrasonic measurements under dry and water-saturated conditions, the drained and unrelaxed (or isolated) regimes are directly attained (Fortin et al., 2014). Following poroelastic theory, this intermediate undrained regime—expected to be that representative of the field measurements (e.g., Adelinet et al., 2018; Pimienta et al., 2018)—can be reached directly by applying Biot-Gassmann equations and assuming isotropic medium to calculate *P* and *S* wave velocities (see Adelinet et al., 2011): The undrained bulk modulus is derived from the drained one and the undrained shear modulus equals the drained one (i.e., measured under dry conditions).

The inferred undrained *P* and *S* wave velocities are compared to the measured values for the two other regimes as a function of ThT temperature (Figure 11). Upon microfracturation as ThT temperature increases, a clear difference is observed between the initially nonporous (Figures 11a–11c) and the initially porous sandstones (Figures 11d and 11e). Consistently with published measurements (Pimienta et al., 2015a, 2015b; Pimienta, Borgomano, et al., 2017), two transitions are observed for the two porous Fontainebleau sandstones. However, interestingly, the undrained and unrelaxed regime fit for the three purely microcracked rocks (i.e., marble, diorite, and granite). It implies that in the three rocks measured, no squirt-flow effects are expected so that *P* wave velocity of the water-saturated cracked samples might be equal in the laboratory and at the field scale. Hence, while large decreases of down to 70% are observed on *P* and *S* wave velocities of all dry rocks in the laboratory, the observation might differ at the field scale if rocks are fully saturated: A maximum decrease of about 40% (i.e., Figures 4b and 4d) is expected for all rock samples.

5. Discussion on Thermal-Induced Microcracking

Although this was not the principal aim of this work, very different rocks were subjected to the same temperature ramps under the exact same experimental conditions. Because the rocks vary in porosity and mineral content, it is of interest to investigate the applicability of commonly used micromechanical models for thermal fracturation. In case of slow temperature variations, the three candidates postulated for thermal cracking are (1) mismatch of thermal expansion between minerals and matrix (Clarke, 1980; Evans & Clarke, 1980; Fredrich & Wong, 1986), (2) minerals anisotropic thermal expansion (Clarke, 1980; Evans & Clarke, 1980; Fredrich & Wong, 1986), and (3) dehydration of the fluid inclusions (Lin, 2002). The latter case was postulated from the presence of fluid inclusions existing in many minerals of granite. Because very similar effects are observed in the different rocks, we disregard this last possibility and discuss the aspects of microfracturing from thermal expansion of the rocks minerals.

5.1. Insights From the Literature

In rocks, studies showed that very different results can be expected depending on the materials and rate of temperature variation—from the slow temperature variations (Richter & Simmons, 1974) to fast thermal quenching (Delle Piane et al., 2015; Ougier-Simonin et al., 2011)—and depending also on the rock type (Fredrich & Wong, 1986). In crustal rocks, slow temperature variations, up to large temperatures, are usually accommodated by minerals thermal expansion and/or phase transformation. In particular, minerals thermoelasticity (i.e., thermal expansion) was shown to induce large degrees of microfracturing (Fredrich & Wong, 1986; Richter & Simmons, 1974; Wong, 1982b; Wong & Brace, 1979). In polymineralic rocks, a mismatch of thermal expansion between minerals and/or between a mineral and the rock matrix (Fredrich & Wong, 1986) was postulated. In monomineralic rocks, because most grains/crystals are anisotropic and with a given orientation, fracturing could occur from anisotropic thermal expansions (Fredrich & Wong, 1986). In the particular case of quartz-rich rocks, the quartz α-β transition (i.e., at about 570 °C) was deemed as a major effect, inducing abrupt and dramatic increases in microcrack densities (Nasseri et al., 2007, 2009). However, in the present case, no abrupt change is observed but rather a progressive variation with increasing ThT. Moreover, the decrease reached its asymptote for values of 550–600 °C, which might imply that once the phase transitions, the maximum degree of microfracturing was already reached.

Most studies investigated granites (Faoro et al., 2013; Fredrich & Wong, 1986; Griffiths et al., 2018; Kern, 1982; Nasseri et al., 2007, 2009; Wang et al., 2013; Wong, 1982a, 1982b; Wong & Brace, 1979), a rock that usually bears a quartz content of about 30%. While strong microfracturing was also observed in some quartzites (Kern, 1982; Mardon et al., 1990), or more recently in marbles (Mahmutoglu, 1998; Peng et al., 2016), much less effects were observed in either basalts and andesites (Bauer & Handin, 1983; Heap et al., 2017; Vinciguerra et al., 2005), calcitic rocks (Fredrich & Wong, 1986; Siddiqi et al., 1997), granodiorite, or diabase (Fredrich & Wong, 1986; Wong & Brace, 1979). Authors further found very different magnitudes of the inhibiting effects of confining pressure on this microfracturation (Bauer & Handin, 1983; Kern, 1982; Siddiqi et al., 1997; Wong & Brace, 1979), which again intrinsically depended on the rock investigated. All of these bring to the need for characterization of the phenomenon, using different rock types of variable mineralogical or porosity contents, thermally treated under the same experimental conditions.

5.2. Thermal Expansion of Minerals

In case of fracturing from thermal expansion (Clarke, 1980; Evans & Clarke, 1980; Fredrich & Wong, 1986), the effects of intergranular (i.e., grain boundary) and intragranular cracking are caused by (i) the mineral sharp edges and (ii) minerals intrinsic thermal expansions. According to earlier works (Fredrich & Wong, 1986), the two phenomena of thermal expansion that could be addressed are of (i) *mismatch*, that is, the difference between the isotropic mineral and surrounding matrix expansions, or (ii) *anisotropic*, that is, the difference between mineral axes of thermal expansions. To account for the problem at hands, and in particular on the effect of the mineral edges, the authors modeled (i.e., square inclusion model) the stress needed for a crack to propagate at the contact between two minerals (Fredrich & Wong, 1986). However, this relies on the existence of an initial crack at the edge between the two minerals, which is not always the case here. Here, following recent works (Passelègue, Spagnuolo, et al., 2016; Wang et al., 2013), we focus on a simplified model (also reported in Fredrich & Wong, 1986) for thermal expansion mismatch of an isotropic mineral inclusion in an isotropic matrix, such that

Table 2
Investigation of the Maximum Values of Anisotropic Δα Possibly Reached Between the Different Minerals by Assuming Again That the Main Quantity to Consider Is That of Difference Between Maximum and Minimum Thermal Expansion Values

Maximum/minimum Thermal expansion (10^{-6} K^{-1})	Quartz $\alpha_{33} = 10$	Microcline $\alpha_{33} = 0.2$	Plagioclase $\alpha_{33} = 3.3$	Calcite $\alpha_{11} = -5.3$
Quartz: $\alpha_{11} = 16.7$	6.7	16.5	13.4	--
Microcline: $\alpha_{11} = 16.3$	6.3	16.2	13	--
Plagioclase: $\alpha_{11} = 6.1$	−3.9	5.9	2.8	--
Calcite: $\alpha_{33} = 26.4$	--	--	--	31.7

$$\Delta \mathbf{S} = \frac{\mathbf{1}}{\mathbf{8\,G_{Ic}}} \frac{\mathbf{E}}{(\mathbf{1-\nu})} (\Delta \boldsymbol{\alpha}\, \Delta \mathbf{T})^{\mathbf{2}}, \tag{5}$$

where ΔS describes the increase in the crack surface as a function of (i) the isotropic expansion mismatch $\Delta\alpha = \alpha_{ii}/3 - \alpha^0$ between the inclusion (α_{ii}) and the matrix (α^0); (ii) the temperature variation applied on the medium ΔT; (iii) the elastic constants, E (i.e., Young's modulus) and ν (i.e., Poisson's ratio), assumed to be equal in the inclusion and the matrix; and (iv) G_{Ic} is the fracture energy. Assuming penny-shaped cracks, ΔS could be defined in terms of crack density (ρ) and average length (c) and then used to infer the increase in crack density (Wang et al., 2013):

$$\boldsymbol{\rho} = \frac{\mathbf{c}}{\mathbf{16\pi G_{Ic}}} \frac{\mathbf{E}}{(\mathbf{1-\nu})} (\Delta \boldsymbol{\alpha}\, \Delta \mathbf{T})^{\mathbf{2}}, \tag{6}$$

The formula relies on additional underlying assumptions: (i) Elastic properties of the inclusion and matrix are assumed to be the same and (ii) cracks propagate only if cracks of length c initially exist in the rock, which are expected to be proportional to the grain size l. Because temperature variations are the same, and effective elastic properties and G_{Ic} are expected to be relatively similar between the rocks studied, the main difference lies in (1) the length of initial cracks c, or alternatively, the grain size, and (2) the difference $\Delta\alpha = \alpha - \alpha^0$.

In the present case, based on the measured P/S wave velocity, the marble, the diorite, and the two blocks of Fontainebleau sandstone did not exhibit apparent initial microcrack density. Hence, although this is usually a theoretical prerequisite for fracture propagation in all micromechanical thermal stress models (Fredrich & Wong, 1986; Siddiqi & Evans, 2015), c is either expected to be zero or to be proportional to the grain size l. The grain size l is similar for the marble, granite, and sandstone samples, of about 200 μm. Hence, the assumption of c being proportional to l may not explain the (i) different variations between marble and other rocks and (ii) the similar dependence between diorite (i.e., $l = 1$ mm), granite, and sandstone (i.e., $l = 200$ μm). As a consequence, independently of the grain size or initial crack content, those temperature dependences may link exclusively to the parameter $\Delta\alpha$. In particular, the temperature dependence implies that $\Delta\alpha$ in all the rocks—except for the marble—is very similar and is much larger in marble.

Expecting for the mismatch to be $\Delta\alpha = \alpha - \alpha^0$, because all rocks' effective thermal expansion α^0 values should fall in the narrow range of $5 - 11\ 10^{-6}$ K^{-1} (Fredrich & Wong, 1986; Wong & Brace, 1979), it would imply for the isotropic α to be much larger for calcite (i.e., marble) and very similar for the other rocks, independently of the mineral content. This does not seem possible, and additionally, Fredrich and Wong (1986) calculated values of (i) $\Delta\alpha_{\text{calc}} = 0$ for calcite-rich rock and (ii) $\Delta\alpha_{\text{qtz}} = 3\ 10^{-6}$ K^{-1} that is more than twice lower than that expected of $7\ 10^{-6}$ K^{-1} (Passelègue, Spagnuolo, et al., 2016; Wang et al., 2013). Moreover, calculating the irreversible thermal expansion mismatch value (equation (6)) from the inverted crack density (Figure 6) yields values of $2 - 3\ 10^{-5}$ K^{-1} at 200 °C for the marble and $2 - 3\ 10^{-6}$ K^{-1} at 400 °C, and around $6 - 7\ 10^{-6}$ K^{-1} beyond 550 °C, for the diorite or Fontainebleau sandstone.

At this point, we recall that all the rocks studied were isotropic at the sample scale because of the random orientation of minerals. Because most minerals are anisotropic, it implies that the anisotropic axes of two grains in contact will seldom have the same orientations. In other words, the axis having much larger thermal expansion of grain 1 (e.g., α_{11}) will be in contact (or at a small angle) with the axis having lower thermal

expansion (e.g., $\alpha_{22} = \alpha_{33}$) of grain 2. Under this consideration, the maximum difference between minerals anisotropic thermal expansion is $\Delta\alpha' = \text{Max}(\alpha_{ii}) - \text{min}(\alpha_{ii})$. For quartz and calcite, one gets $\Delta\alpha'_{qtz} = 6.7\times 10^{-6}\ \text{K}^{-1}$ and $\Delta\alpha'_{\text{calc}} = 31.7\times10^{-6}\ \text{K}^{-1}$ (Table 2). Thus, consistent with the irreversible expansion inferred from the data, replacing $\Delta\alpha$ by $\Delta\alpha'$ in equation (1) would explain better the large differences between marble and sandstones. For the granite, such value of $6-7\ 10^{-6}\ \text{K}^{-1}$ could be reached for a dominance of contacts between quartz or microcline maximum α_{11} and quartz minimum α_{33}. For the diorite, similar to the Fredrich diabase (Fredrich & Wong, 1986), a dominance of plagioclase contacts might occur, consistently yielding values of about $2-3\ 10^{-6}\ \text{K}^{-1}$.

6. Conclusions

Five rock types of varying mineral content and initial porosity have been subjected to various temperatures of treatment to investigate the effect of microfracturing on the links between effective properties. The samples pore and bulk volumes, ultrasonic velocities, and electrical impedance have been measured before and after ThT. For all rocks, an increase in temperature of treatment leads to (i) an increase in pore and bulk volume, (ii) a decrease in ultrasonic wave velocities, and (iii) a decrease in formation factor. From ultrasonic wave velocities, the created porosity is of thin and elongated microcracks, which also leads to a large decrease in the electrical formation factor. From the phase shift of the electrical impedance data, large variations in phase peak amplitudes are observed that correlate with the porosity variations. The crack density inverted from *P* wave velocities allows for inferring permeability values that are consistent with that inferred from electrical formation factor.

From both the crack porosity and electrical impedance data, the major effect is of creation or propagation of cracks (i.e., crack density increase) rather than its aspect ratio. Because electrical impedance evidences an increase in the cracks opening with ThT, this might imply that both opening and length vary in the same way. Accounting for the frequency of measurement at the field scale, the effect of microcracking is surprisingly very similar for all rock samples, hence independent of initially existing or created porosity. Finally, apart from Rothbach sandstone, very different behaviors are observed in the marble as compared to the other rocks, and very similar variations are observed in all other rocks independently of the (i) grain size, (ii) initial porosity, or (iii) initial content of crack. Comparing it with a simple model, rather than expansion mismatch, anisotropic thermal expansion of the minerals might explain those variations.

Appendix A: Elastic Model and Cracks Interaction

The model chosen predicts the effective compliance of a homogenous medium in which a family of thin elongated spheroidal cracks is introduced through its added compliance (E. C. David & Zimmerman, 2011; Guéguen & Kachanov, 2011; Kachanov, 1993); that is, assuming that once all cracks are closed, the medium behaves as a pure homogeneous medium. Using such model requires the knowledge of the elastic properties of the medium when all cracks are closed (Wang et al., 2013), for example, at High Confining Pressures (e.g., HCP medium in Figure (2) of Pimienta, Sarout, et al., 2014). Because we specifically chose rocks with low initial degree of crack densities, for all samples except the granite and Rothbach sandstone, the initial properties for all modeled homogeneous media are that measure on the nontreated samples. For Rothbach sandstone, porosity is very large and open grain contacts might remain, hence making the rock not very applicable for these studies specific to cracks in nonporous rocks. For the granite, an initial microcrack density might have already been present (i.e., low V_p and V_s in Table 1). The properties chosen are that reported at high confining pressure (Wang et al., 2013), when all cracks are closed.

The inclusion models intrinsically depend both on (i) how the compliance of an inclusion affects the matrix effective compliance and (ii) how the different inclusions interact between themselves (Guéguen & Kachanov, 2011; Kachanov, 1993). The absolute value of inverted crack density is thus model dependent. To sum the effect of cracks compliance, the simplest and more robust (Guéguen & Kachanov, 2011; Kachanov, 1993) Non Interaction Approximation is often used (Adelinet et al., 2011; Fortin et al., 2007; Nasseri et al., 2007, 2009). In case of elongated spheroidal cracks, it yields effective properties (K_{eff} and G_{eff}) of the isotropic rock so that (Fortin et al., 2007; Kachanov, 1993; Pimienta, Sarout, et al., 2014):

$$\begin{cases} \dfrac{K_m}{K_{eff}} = 1 + \rho \dfrac{16\left(1-\upsilon_m^2\right)}{9\,(1-2\upsilon_m)} \dfrac{\delta_c}{1+\delta_c} \\ \dfrac{G_m}{G_{eff}} = 1 + \rho \dfrac{16}{15}\left[\dfrac{(1-\upsilon_m)}{(2-\upsilon_m)} + \dfrac{2}{3}(1-\upsilon_m)\dfrac{\delta_c}{1+\delta_c}\right] \end{cases}, \tag{A1}$$

where ρ is the density of cracks embedded in the mineral background and δ_c accounts for the fluid compressibility (K_f) and the cracks geometry of an aspect ratio ξ, such that

$$\delta_c = \rho \frac{\pi \xi}{4} \frac{E_m}{\left(1-\upsilon_m^2\right)} \left(\frac{1}{K_f} - \frac{1}{K_m}\right). \tag{A2}$$

where K_m, G_m, E_m, and υ_m are the bulk modulus, shear modulus, Young's modulus, and Poisson's ratio of the HCP medium in which cracks are embedded. For an isotropic medium, only two elastic constants are independent so that E_m and υ_m can directly be inferred from K_m and G_m. From K_{eff} and G_{eff}) one gets the effective P wave velocity of the cracked medium. Using this model, however, yields ρ values as high as about 4–5 at maximum ThT. While this is very similar to what was already inferred in the literature (Nasseri et al., 2009), this is not realistic as a value of 1 would theoretically link to the sample fragmentation.

The reason is that because the Non Interaction Approximation method does not account for the mechanical interaction between cracks, it largely overestimates the density of cracks (Nasseri et al., 2007, 2009; Pimienta, Sarout, et al., 2014). The Differential Effective Medium approximation is expected to better account for this interaction (E. C. David & Zimmerman, 2011, 2012), which might decrease the overestimation made on the crack density (Guéguen & Kachanov, 2011; Pimienta et al., 2018). Based on equation (1), we use here a discrete form of the Differential Effective Medium approximation (Pimienta et al., 2018) to build the effective model (K_{eff} and G_{eff}) and then infer the effective P wave velocity of this isotropic medium.

Acknowledgments
The authors are very thankful to the two reviewers and wish to acknowledge their important work in tracking typos and greatly improve the rationale of this contribution. All the data sets presented in the figures are reported as supporting information. This work was allowed by the support for the EPFL and Marie Curie Fellowship of L. P., by the MSCA (PROGRESS, project 665667) and the Swiss Competence Center for Energy Research (SCCER). M. V. thanks the European Research Council through the Starting Grant project 757290-BEFINE. We thank Dr. Thierry Adatte for XRD measurements.

References

Adelinet, M., Domínguez, C., Fortin, J., & Violette, S. (2018). Seismic-refraction field experiments on Galapagos Islands: A quantitative tool for hydrogeology. *Journal of Applied Geophysics*, *148*, 139–151. https://doi.org/10.1016/j.jappgeo.2017.10.009

Adelinet, M., Fortin, J., & Guéguen, Y. (2011). Dispersion of elastic moduli in a porous-cracked rock: Theoretical predictions for squirt-flow. *Tectonophysics*, *503*(1–2), 173–181. https://doi.org/10.1016/j.tecto.2010.10.012

Archie, G. E. (1941). The electrical resistivity log as an aid in determining some reservoir characteristics. *Transactions of AIME*, *146*(01), 54–62.

Archie, G. E. (1952). Classification of carbonate reservoir rocks and petrophysical considerations. *AAPG Bulletin*, *36*(2), 278–298.

Bauer, S. J., & Handin, J. (1983). Thermal expansion and cracking of three confined water-saturated igneous rocks to 800 °C. *Rock Mechanics and Rock Engineering*, *16*(3), 181–198. https://doi.org/10.1007/BF01033279

Benson, P. M., Meredith, P. G., & Schubnel, A. (2006). Role of void space geometry in permeability evolution in crustal rocks at elevated pressure. *Journal of Geophysical Research*, *111*, B12203. https://doi.org/10.1029/2006JB004309

Benson, P. M., Schubnel, A., Vinciguerra, S., Trovato, C., Meredith, P., & Young, R. P. (2006). Modeling the permeability evolution of microcracked rocks from elastic wave velocity inversion at elevated isostatic pressure. *Journal of Geophysical Research*, *111*, B04202. https://doi.org/10.1029/2005JB003710

Bernabé, Y. (1991). Pore geometry and pressure dependence of the transport pproperties in sandstones. *Geophysics*, *56*(4), 436–446. https://doi.org/10.1190/1.1443061

Bourbie, T., & Zinszner, B. (1985). Hydraulic and acoustic properties as a function of porosity in Fontainebleau sandstone. *Journal of Geophysical Research*, *90*(B13), 11,524–11,532.

Bourbié, T., & Zinszner, B. (1985). Hydraulic and acoustic properties as a function of porosity in Fontainebleau Sandstone. *Journal of Geophysical Research*, *90*(B13), 11,524–11,532. https://doi.org/10.1029/JB090iB13p11524

Brace, W. F. (1965a). Relation of elastic properties of rocks to fabric. *Journal of Geophysical Research*, *70*(22), 5657–5667. https://doi.org/10.1029/JZ070i022p05657

Brace, W. F. (1965b). Some new measurements of linear compressibility of rocks. *Journal of Geophysical Research*, *70*(2), 391–398. https://doi.org/10.1029/JZ070i002p00391

Brace, W. F. (1977). Permeability from resistivity and pore shape. *Journal of Geophysical Research*, *82*(23), 3343–3349. https://doi.org/10.1029/JB082i023p03343

Brace, W. F., Orange, A. S., & Madden, T. B. (1965). The effect of pressure on the electrical resistivity of water-saturated crystalline rocks. *Journal of Geophysical Research*, *70*(22), 5669–5678. https://doi.org/10.1029/JZ070i022p05669

Brace, W. F., Walsh, J. B., & Frangos, W. T. (1968). Permeability of granite under high pressure. *Journal of Geophysical Research*, *73*(6), 2225–2236. https://doi.org/10.1029/JB073i006p02225

Cai, J., Wei, W., Hu, X., & Wood, D. A. (2017). Electrical conductivity models in saturated porous media: A review. *Earth-Science Reviews*, *171*(June), 419–433. https://doi.org/10.1016/j.earscirev.2017.06.013

Casteleyn, L., Robion, P., David, C., Collin, P. Y., Menéndez, B., Fernandes, N., et al. (2011). An integrated study of the petrophysical properties of carbonate rocks from the "Oolithe Blanche" formation in the Paris Basin. *Tectonophysics*, *503*(1–2), 18–33. https://doi.org/10.1016/j.tecto.2010.09.031

Clarke, D. R. (1980). Microfracture in brittle solids resulting from anisotropic shape changes. *Acta Metallurgica*, *28*(7), 913–924. https://doi.org/10.1016/0001-6160(80)90107-8

Clennell, B. (2010). Electrical properties of sedimentary rocks from DC to dielectric frequencies, (June).
Daily, W. D., & Lin, W. (1985). Laboratory-determined transport properties of Berea sandstone. *Geophysics*, *50*(5), 775–784. https://doi.org/10.1190/1.1441952
David, C., Darot, M., & Jeannette, D. (1993). Pore structures and transport properties of sandstone. *Transport in Porous Media*, *11*(2), 161–177. https://doi.org/10.1007/BF01059632
David, C., Menendez, B., Zhu, W., & Wong, T. (2001). Mechanical compaction, microstructures and permeability evolution in sandstones. *Physics and Chemistry of the Earth, Part A: Solid Earth and Geodesy*, *26*(1–2), 45–51. https://doi.org/10.1016/S1464-1895(01)00021-7
David, C., Wassermann, J., Amann, F., Klaver, J., Davy, C., Sarout, J., et al. (2018). KG^{2}B, a collaborative benchmarking exercise for estimating the permeability of the Grimsel granodiorite—Part 2: Modelling, microstructures and complementary data. *Geophysical Journal International*, *215*(2), 825–843. https://doi.org/10.1093/gji/ggy305
David, C., Wong, T., Zhu, W., & Zhang, J. (1994). Laboratory measurement of compaction-induced permeability change in porous rocks: Implications for the generation and maintenance of pore pressure excess in the crust. *Pure and Applied Geophysics PAGEOPH*, *143*(1-3), 425–456. https://doi.org/10.1007/BF00874337
David, E. C., & Zimmerman, R. W. (2011). Compressibility and shear compliance of spheroidal pores: Exact derivation via the Eshelby tensor, and asymptotic expressions in limiting cases. *International Journal of Solids and Structures*, *48*(5), 680–686. https://doi.org/10.1016/j.ijsolstr.2010.11.001
David, E. C., & Zimmerman, R. W. (2012). Pore structure model for elastic wave velocities in fluid-saturated sandstones. *Journal of Geophysical Research*, *117*, B07210. https://doi.org/10.1029/2012JB009195
Davidge, R. W., & Green, T. J. (1968). The strength of two-phase ceramic/glass materials. *Journal of Materials Science*, *3*(6), 629–634. https://doi.org/10.1007/BF00757910
Delle Piane, C., Arena, A., Sarout, J., Esteban, L., & Cazes, E. (2015). Micro-crack enhanced permeability in tight rocks: An experimental and microstructural study. *Tectonophysics*, *665*, 149–156. https://doi.org/10.1016/j.tecto.2015.10.001
Eberhart-Phillips, D., Stanley, W. D., Rodriguez, B. D., & Lutter, W. J. (1995). Surface seismic and electrical methods to detect fluids related to faulting. *Journal of Geophysical Research*, *100*, 12,919–12,936.
Evans, A. G., & Clarke, D. R. (1980). Residual stresses and microcracking induced by thermal contraction inhomogeneity. In D. P. H. Hasselman, & R. A. Heller (Eds.), *Thermal Stresses in severe environments*, (pp. 451–460). Boston, MA: Springer. https://doi.org/10.1038/ismej.2011.91
Faoro, I., Vinciguerra, S., Marone, C., Elsworth, D., & Schubnel, A. (2013). Linking permeability to crack density evolution in thermally stressed rocks under cyclic loading. *Geophysical Research Letters*, *40*, 2590–2595. https://doi.org/10.1002/grl.50436
Fortin, J., Guéguen, Y., & Schubnel, A. (2007). Effects of pore collapse and grain crushing on ultrasonic velocities and Vp/Vs. *Journal of Geophysical Research*, *112*, B08207. https://doi.org/10.1029/2005JB004005
Fortin, J., Pimienta, L., Guéguen, Y., Schubnel, A., David, E. C., & Adelinet, M. (2014). Experimental results on the combined effects of frequency and pressure on the dispersion of elastic waves in porous rocks. *The Leading Edge*, *33*(6), 648–654. https://doi.org/10.1190/tle33060648.1
Fredrich, J. T., & Wong, T. (1986). Micromechanics of thermally induced cracking in threee crustal rocks. *Journal of Geophysical Research*, *91*(B12), 12,743–12,764. https://doi.org/10.1029/JB091iB12p12743
Glover, P. W. J., Hole, M. J., & Pous, J. (2000). A modified Archie's law for two conducting phases. *Earth and Planetary Science Letters*, *180*(3–4), 369–383. https://doi.org/10.1016/S0012-821X(00)00168-0
Gomez, C. T., Dvorkin, J., & Vanorio, T. (2010). Laboratory measurements of porosity, permeability, resistivity, and velocity on Fontainebleau sandstones. *Geophysics*, *75*(6), E191–E204. https://doi.org/10.1190/1.3493633
Griffiths, L., Heap, M. J., Baud, P., & Schmittbuhl, J. (2017). Quantification of microcrack characteristics and implications for stiffness and strength of granite. *International Journal of Rock Mechanics and Mining Sciences*, *100*, 138–150. https://doi.org/10.1016/j.ijrmms.2017.10.013
Griffiths, L., Lengliné, O., Heap, M. J., Baud, P., & Schmittbuhl, J. (2018). Thermal cracking in Westerly Granite monitored using direct wave velocity, coda wave interferometry and acoustic emissions. *Journal of Geophysical Research: Solid Earth*, *123*, 2246–2261. https://doi.org/10.1002/2017JB015191
Guéguen, Y., & Dienes, J. (1989). Transport properties of rocks from statistics and percolation. *Mathematical Geology*, *21*(1), 1–13. https://doi.org/10.1007/BF00897237
Guéguen, Y., & Kachanov, M. (2011). *Effective elastic properties of cracked rocks: An overview. Mechanics of Crustal Rocks* (pp. 73–125). Vienna: Springer.
Guéguen, Y., & Palciauskas, V. (1994). *Introduction to the physics of rocks*. Princeton, N.J.: Princeton University Press.
Guéguen, Y., Sarout, J., Fortin, J., & Schubnel, A. (2009). Cracks in porous rocks: Tiny defects, strong effects. *The Leading Edge*, *28*(1), 40–47. https://doi.org/10.1190/1.3064145
Gurevich, B., & Makarynska, D. (2012). Rigorous bounds for seismic dispersion and attenuation due to wave-induced fluid flow in porous rocks. *Geophysics*, *77*(6), L45–L51. https://doi.org/10.1190/geo2012-0039.1
Gurevich, B., Makarynska, D., de Paula, O. B., & Pervukhina, M. (2010). A simple model for squirt-flow dispersion and attenuation in fluid-saturated granular rocks. *Geophysics*, *75*(6), N109–N120. https://doi.org/10.1190/1.3509782
Han, M., Youssef, S., Rosenberg, E., Fleury, M., & Levitz, P. (2009). Deviation from Archie's law in partially saturated porous media: Wetting film versus disconnectedness of the conducting phase. *Physical Review E - Statistical, Nonlinear, and Soft Matter Physics*, *79*(3), 1–11. https://doi.org/10.1103/PhysRevE.79.031127
Han, T. (2018). Joint elastic-electrical properties of artificial porous sandstone with aligned fractures. *Geophysical Research Letters*, *45*, 3051–3058. https://doi.org/10.1002/2018GL077541
Han, T., Best, A. I., MacGregor, L. M., Sothcott, J., & Minshull, T. A. (2011). Joint elastic-electrical effective medium models of reservoir sandstones. *Geophysical Prospecting*, *59*(4), 777–786. https://doi.org/10.1111/j.1365-2478.2011.00956.x
Han, T., Best, A. I., Sothcott, J., & Macgregor, L. M. (2011). Pressure effects on the joint elastic-electrical properties of reservoir sandstones. *Geophysical Prospecting*, *59*(3), 506–517. https://doi.org/10.1111/j.1365-2478.2010.00939.x
Han, T., Clennell, M. B., Josh, M., & Pervukhina, M. (2015). Determination of effective grain geometry for electrical modeling of sedimentary rocks. *Geophysics*, *80*(4), D319–D327. https://doi.org/10.1190/geo2014-0504.1
Heap, M. J., Baud, P., & Meredith, P. G. (2009). Influence of temperature on brittle creep in sandstones. *Geophysical Research Letters*, *36*, L19305. https://doi.org/10.1029/2009GL039373

Heap, M. J., Violay, M., Wadsworth, F. B., & Vasseur, J. (2017). From rock to magma and back again: The evolution of temperature and deformation mechanism in conduit margin zones. *Earth and Planetary Science Letters*, *463*, 92–100. https://doi.org/10.1016/j.epsl.2017.01.021

Heuze, F. E. (1983). High-temperature mechanical, physical and thermal properties of granitic rocks—A review. *International Journal of Rock Mechanics and Mining Sciences And*, *20*(1), 3–10. https://doi.org/10.1016/0148-9062(83)91609-1

Jouniaux, L., Bernard, M. L., Zamora, M., & Pozzi, J. P. (2000). Streaming potential in volcanic rocks from Mount Pelee. *Journal of Geophysical Research*, *105*(B4), 8391–8401. https://doi.org/10.1029/1999JB900435

Jouniaux, L., Maineult, A., Naudet, V., Pessel, M., & Sailhac, P. (2009). Review of self-potential methods in hydrogeophysics. *Comptes Rendus Geoscience*, *341*(10–11), 928–936. https://doi.org/10.1016/j.crte.2009.08.008

Jouniaux, L., & Pozzi, J. (1995). Permeability dependence of streaming potential in rocks for various fluid conductivities. *Geophysical Research Letters*, *22*(4), 485–488.

Kachanov, M. (1993). Elastic solids with many cracks and related problems. *Advances in Applied Mechanics*, *30*, 259–445. https://doi.org/10.1016/S0065-2156(08)70176-5

Kern, H. (1982). Elastic-wave velocity in crustal and mantle rocks at high pressure and temperature: The role of the high-low quartz transition and of dehydration reactions. *Physics of the Earth and Planetary Interiors*, *29*(1), 12–23. https://doi.org/10.1016/0031-9201(82)90133-9

Knight, R. J., & Dvorkin, J. (1992). Seismic and electrical properties of sandstones at low saturations. *Journal of Geophysical Research*, *97*(B12), 17,417–17,425.

Knight, R. J., Nolte, L. J. P., Slater, L., Atekwana, E., Endres, A., Geller, J., et al. (2010). Geophysics at the interface: Response of geophysical properties to solid-fluid, fluid-fluid, and solid-solid interfaces. *Reviews of Geophysics*, *48*, RG4002. https://doi.org/10.1029/2007RG000242

Le Ravalec, M., & Guéguen, Y. (1996). High-and low-frequency elastic moduli for a saturated porous/cracked rock—Differential self-consistent and poroelastic theories. *Geophysics*, *61*(4), 1080–1094. https://doi.org/10.1190/1.1444029

Lesmes, D. P., & Friedman, S. P. (2005). Relationships between the electrical and hydrogeological properties of rocks and soils. *Hydrogeophysics*, 87–128. https://doi.org/10.1007/1-4020-3102-5_4

Lesmes, D. P., & Frye, K. . K. M. (2001). Influence of pore fluid chemistry on the complex conductivity and induced polarization responses of Berea sandstone. *Journal of Geophysical Research*, *106*(B3), 4079–4090. https://doi.org/10.1029/2000JB900392

Lin, W. (2002). Permanent strain of thermal expansion and thermally induced microcracking in Inada granite. *Journal of Geophysical Research*, *107*(B10), 2215. https://doi.org/10.1029/2001JB000648

Louis, L., Baud, P., & Wong, T. F. (2009). Microstructural inhomogeneity and mechanical anisotropy associated with bedding in rothbach sandstone. *Pure and Applied Geophysics*, *166*(5–7), 1063–1087. https://doi.org/10.1007/s00024-009-0486-1

Louis, L., Wong, T. F., & Baud, P. (2007). Imaging strain localization by X-ray radiography and digital image correlation: Deformation bands in Rothbach sandstone. *Journal of Structural Geology*, *29*(1), 129–140. https://doi.org/10.1016/j.jsg.2006.07.015

Mahmutoglu, Y. (1998). Mechanical behaviour of cyclically heated fine grained rock. *Rock Mechanics and Rock Engineering*, *31*(3), 169–179. https://doi.org/10.1007/s006030050017

Maineult, A., Jougnot, D., & Revil, A. (2018). Variations of petrophysical properties and spectral induced polarization in response to drainage and imbibition: A study on a correlated random tube network. *Geophysical Journal International*, *212*(2), 1398–1411. https://doi.org/10.1093/gji/ggx474

Mardon, D., Kronenberg, A. K., Handin, J., Friedman, M., & Russell, J. E. (1990). Mechanisms of fracture propagation in experimentally extended Sioux quartzite. *Tectonophysics*, *182*(3–4), 259–278. https://doi.org/10.1016/0040-1951(90)90167-7

Mavko, G., Mukerji, T., & Dvorkin, J. (2003). *The rock physics handbook: Tools for seismic analysis of porous media*. Cambridge: Cambridge University Press.

Milsch, H., Kristinsdóttir, L. H., Spangenberg, E., Bruhn, D., & Flóvenz, Ó. G. (2010). Effect of the water-steam phase transition on the electrical conductivity of porous rocks. *Geothermics*, *39*(1), 106–114. https://doi.org/10.1016/j.geothermics.2009.09.001

Müller, T. M., Gurevich, B., & Lebedev, M. (2010). Seismic wave attenuation and dispersion resulting from wave-induced flow in porous rocks—A review. *Geophysics*, *75*(5), 75A147–75A164. https://doi.org/10.1190/1.3463417

Nara, Y., Meredith, P. G., Yoneda, T., & Kaneko, K. (2011). Influence of macro-fractures and micro-fractures on permeability and elastic wave velocities in basalt at elevated pressure. *Tectonophysics*, *503*(1–2), 52–59. https://doi.org/10.1016/j.tecto.2010.09.027

Nasseri, M. H. B., Schubnel, A., Benson, P. M., & Young, R. P. (2009). Common evolution of mechanical and transport properties in thermally cracked westerly granite at elevated hydrostatic pressure. *Pure and Applied Geophysics*, *166*(5–7), 927–948. https://doi.org/10.1007/s00024-009-0485-2

Nasseri, M. H. B., Schubnel, A., & Young, R. P. (2007). Coupled evolutions of fracture toughness and elastic wave velocities at high crack density in thermally treated Westerly granite. *International Journal of Rock Mechanics and Mining Sciences*, *44*(4), 601–616. https://doi.org/10.1016/j.ijrmms.2006.09.008

O'Connell, R. J., & Budiansky, B. (1977). Viscoelastic properties of fluid-saturated cracked solids. *Journal of Geophysical Research*, *82*(36), 5719–5735. https://doi.org/10.1029/JB082i036p05719

Ougier-Simonin, A., Fortin, J., Guéguen, Y., Schubnel, A., & Bouyer, F. (2011). Cracks in glass under triaxial conditions. *International Journal of Engineering Science*, *49*(1), 105–121. https://doi.org/10.1016/j.ijengsci.2010.06.026

Passelègue, F. X., Schubnel, A., Nielsen, S., Bhat, H. S., Deldicque, D., & Madariaga, R. (2016). Dynamic rupture processes inferred from laboratory microearthquakes. *Journal of Geophysical Research: Solid Earth*, *121*, 4343–4365. https://doi.org/10.1002/2015JB012694

Passelègue, F. X., Spagnuolo, E., Violay, M., Nielsen, S., Di Toro, G., & Schubnel, A. (2016). Frictional evolution, acoustic emissions activity, and off-fault damage in simulated faults sheared at seismic slip rates. *Journal of Geophysical Research: Solid Earth*, *121*, 7490–7513. https://doi.org/10.1002/2016JB012988

Peng, J., Rong, G., Cai, M., Di Yao, M., & Zhou, C. B. (2016). Physical and mechanical behaviors of a thermal-damaged coarse marble under uniaxial compression. *Engineering Geology*, *200*, 88–93. https://doi.org/10.1016/j.enggeo.2015.12.011

Pimienta, L., Borgomano, J. V. M., Fortin, J., & Guéguen, Y. (2017). Elastic dispersion and attenuation in fully saturated sandstones: Role of mineral content, porosity and pressures. *Journal of Geophysical Research: Solid Earth*, *122*, 9950–9965. https://doi.org/10.1002/2017JB014645

Pimienta, L., Fortin, J., Borgomano, J. V. M., & Guéguen, Y. (2016). Dispersions and attenuations in a fully saturated sandstone: Experimental evidence for fluid flows at different scales. *The Leading Edge*, *35*(6), 495–501. https://doi.org/10.1190/tle35060495.1

Pimienta, L., Fortin, J., & Gueguen, Y. (2014). Investigation of elastic weakening in limestone and sandstone samples from moisture adsorption. *Geophysical Journal International*, *199*(1), 335–347. https://doi.org/10.1093/gji/ggu257

Pimienta, L., Fortin, J., & Guéguen, Y. (2015a). Bulk modulus dispersion and attenuation in sandstones. *Geophysics*, *80*(2), D111–D127. https://doi.org/10.1190/geo2014-0335.1

Pimienta, L., Fortin, J., & Guéguen, Y. (2015b). Experimental study of Young's modulus dispersion and attenuation in fully saturated sandstones. *Geophysics*, *80*(5), L57–L72. https://doi.org/10.1190/geo2014-0532.1

Pimienta, L., Sarout, J., Esteban, L., David, C., & Clennell, M. B. (2017). Pressure-dependent elastic and transport properties of porous and permeable rocks: Microstructural control. *Journal of Geophysical Research: Solid Earth*, *122*, 8952–8968. https://doi.org/10.1002/2017JB014464

Pimienta, L., Sarout, J., Esteban, L., & Piane, C. D. (2014). Prediction of rocks thermal conductivity from elastic wave velocities, mineralogy and microstructure. *Geophysical Journal International*, *197*(2), 860–874. https://doi.org/10.1093/gji/ggu034

Pimienta, L., Schubnel, A., Violay, M., Fortin, J., Guéguen, Y., & Lyon-Caen, H. (2018). Anomalous Vp/Vs ratios at seismic frequencies might evidence highly damaged rocks in subduction zones. *Geophysical Research Letters*, *45*(22), 210–217. https://doi.org/10.1029/2018GL080132

Ramez, M. R. H., & Murrell, S. A. F. (1964). A petrofabric analysis of Carrara marble. *International Journal of Rock Mechanics and Mining Sciences*, *1*(2), 217–229. https://doi.org/10.1016/0148-9062(64)90028-2

Reuschlé, T., Gbaguidi Haore, S., & Darot, M. (2003). Microstructural control on the elastic properties of thermally cracked granite. *Tectonophysics*, *370*(1–4), 95–104. https://doi.org/10.1016/S0040-1951(03)00179-3

Revil, A. (2013). Effective conductivity and permittivity of unsaturated porous materials in the frequency range 1 mHz-1GHz. *Water Resources Research*, *49*, 306–327. https://doi.org/10.1029/2012WR012700

Revil, A., Binley, A., Mejus, L., & Kessouri, P. (2015). Predicting permeability from the characteristic relaxation time and intrinsic formation factor of complex conductivity spectra. *Water Resources Research*, *51*, 1649–1670. https://doi.org/10.1002/2014WR016259

Revil, A., Kessouri, P., & Torres-Verdín, C. (2014). Electrical conductivity, induced polarization, and permeability of the Fontainebleau sandstone. *Geophysics*, *79*(5), D301–D318. https://doi.org/10.1190/geo2014-0036.1

Revil, A., Koch, K., & Holliger, K. (2012). Is it the grain size or the characteristic pore size that controls the induced polarization relaxation time of clean sands and sandstones? *Water Resources Research*, *48*, W05602. https://doi.org/10.1029/2011WR011561

Rice, J. R., & Cleary, M. P. (1976). Some basic stress diffusion solutions for fluid-saturated elastic porous media with compressible constituents. *Reviews of Geophysics*, *14*(2), 227–241. https://doi.org/10.1029/RG014i002p00227

Richter, D., & Simmons, G. (1974). Thermal expansion behavior of igneous rocks. *International Journal of Rock Mechanics and Mining Sciences*, *11*(10), 403–411. https://doi.org/10.1016/0148-9062(74)91111-5

Sarout, J. (2012). Impact of pore space topology pn permeability, cut-off frequencies and validity of wave propagation theories. *Geophysical Journal International*, *189*(1), 481–492. https://doi.org/10.1111/j.1365-246X.2011.05329.x

Sarout, J., Cazes, E., Delle Piane, C., Arena, A., & Esteban, L. (2017). Stress-dependent permeability and wave dispersion in tight cracked rocks: Experimental validation of simple effective medium models. *Journal of Geophysical Research: Solid Earth*, *122*, 6180–6201. https://doi.org/10.1002/2014JB011736

Schubnel, A., Benson, P. M., Thompson, B. D., Hazzard, J. F., & Young, R. P. (2006). Quantifying damage, saturation and anisotropy in cracked rocks by inverting elastic wave velocities. *Pure and Applied Geophysics*, *163*(5–6), 947–973. https://doi.org/10.1007/s00024-006-0061-y

Schubnel, A., Fortin, J., Burlini, L., & Guéguen, Y. (2005). Damage and recovery of calcite rocks deformed in the cataclastic regime. *Geological Society, London, Special Publications*, *245*(1), 203–221. https://doi.org/10.1144/GSL.SP.2005.245.01.10

Schubnel, A., Walker, E., Thompson, B. D., Fortin, J., Guéguen, Y., & Young, R. P. (2006). Transient creep, aseismic damage and slow failure in Carrara marble deformed across the brittle-ductile transition. *Geophysical Research Letters*, *33*, L17301. https://doi.org/10.1029/2006GL026619

Sen, P. N. (1997). Resistivity of partially saturated carbonate rocks with microporosity. *Geophysics*, *62*(2), 415–425. https://doi.org/10.1190/1.1444152

Siddiqi, G., & Evans, B. (2015). Permeability and thermal cracking at pressure in Sioux Quartzite. *Geological Society, London, Special Publications*, *409*(1), 49–66. https://doi.org/10.1144/SP409.11

Siddiqi, G., Evans, B., Dresen, G., & Freund, D. (1997). Effect of semibrittle deformation on transport properties of calcite rocks. *Journal of Geophysical Research*, *102*(B7), 14,765–14,778. https://doi.org/10.1029/97JB01038

Simmons, G., & Brace, W. F. (1965). Comparison of static and dynamic measurements of compressibility of rocks. *Journal of Geophysical Research*, *70*(22), 5649–5656. https://doi.org/10.1029/JZ070i022p05649

Slater, L. D., & Lesmes, D. (2002). IP interpretation in environmental investigations. *Geophysics*, *67*(1), 77–88. https://doi.org/10.1190/1.1451353

Sondergeld, C. H., & Estey, L. H. (1981). Acoustic emission study of microfracturing during the cyclic loading of Westerly granite. *Journal of Geophysical Research*, *86*(B4), 2915–2924. https://doi.org/10.1029/JB086iB04p02915

Song, I., & Renner, J. (2006). Experimental investigation into the scale dependence of fluid transport in heterogeneous rocks. *Pure and Applied Geophysics*, *163*(10), 2103–2123. https://doi.org/10.1007/s00024-006-0121-3

Song, I., & Renner, J. (2008). Hydromechanical properties of Fontainebleau sandstone: Experimental determination and micromechanical modeling. *Journal of Geophysical Research*, *113*, B09211. https://doi.org/10.1029/2007JB005055

Sun, W. C., & Wong, T. f. (2018). Prediction of permeability and formation factor of sandstone with hybrid lattice Boltzmann/finite element simulation on microtomographic images. *International Journal of Rock Mechanics and Mining Sciences*, *106*(April), 269–277. https://doi.org/10.1016/j.ijrmms.2018.04.020

Thompson, B. D., Young, R. P., & Lockner, D. A. (2006). Fracture in Westerly granite under AE feedback and constant strain rate loading: Nucleation, quasi-static propagation, and the transition to unstable fracture propagation. *Pure and Applied Geophysics*, *163*(5–6), 995–1019. https://doi.org/10.1007/s00024-006-0054-x

Tirado, M. C., Arroyo, F. J., Delgado, A. V., & Grosse, C. (2000). Measurement of the low-frequency dielectric properties of colloidal suspensions: Comparison between different methods. *Journal of Colloid and Interface Science*, *227*(1), 141–146. https://doi.org/10.1006/jcis.2000.6825

Titov, K., Tarasov, A., Ilyin, Y., Seleznev, N., & Boyd, A. (2010). Relationships between induced polarization relaxation time and hydraulic properties of sandstone. *Geophysical Journal International*, *180*(3), 1095–1106. https://doi.org/10.1111/j.1365-246X.2009.04465.x

Tong, M., Li, L., Wang, W., & Jiang, Y. (2006). A time-domain induced-polarization method for estimating permeability in a shaly sand reservoir. *Geophysical Prospecting*, *54*(5), 623–631. https://doi.org/10.1111/j.1365-2478.2006.00568.x

Vinciguerra, S., Trovato, C., Meredith, P. G., & Benson, P. M. (2005). Relating seismic velocities, thermal cracking and permeability in Mt. Etna and Iceland basalts. *International Journal of Rock Mechanics and Mining Sciences*, *42*(7-8), 900–910. https://doi.org/10.1016/j.ijrmms.2005.05.022

Violay, M., Gibert, B., Azais, P., Pezard, P. A., & Lods, G. (2012). A new cell for electrical conductivity measurement on saturated samples at upper crust conditions. *Transport in Porous Media*, *91*(1), 303–318. https://doi.org/10.1007/s11242-011-9846-2

Walsh, J. B. (1965a). The effect of cracks in rocks on Poisson's ratio. *Journal of Geophysical Research*, *70*(20), 5249–5257. https://doi.org/10.1029/JZ070i020p05249

Walsh, J. B. (1965b). The effect of cracks on the compressibility of rock. *Journal of Geophysical Research*, *70*(2), 381–389. https://doi.org/10.1029/JZ070i002p00381

Walsh, J. B. (1965c). The effect of cracks on the uniaxial elastic compression of rocks. *Journal of Geophysical Research*, *70*(2), 399–411. https://doi.org/10.1029/JZ070i002p00399

Walsh, J. B., & Brace, W. F. (1984). The effect of pressure on porosity and the transport properties of rock. *Journal of Geophysical Research*, *89*(B11), 9425–9431. https://doi.org/10.1029/JB089iB11p09425

Wang, X. Q., Schubnel, A., Fortin, J., David, E. C., Guéguen, Y., & Ge, H.-K. (2012). High Vp/Vs ratio: Saturated cracks or anisotropy effects? *Geophysical Research Letters*, *39*, L11307. https://doi.org/10.1029/2012GL051742

Wang, X. Q., Schubnel, A., Fortin, J., Guéguen, Y., & Ge, H. K. (2013). Physical properties and brittle strength of thermally cracked granite under confinement. *Journal of Geophysical Research: Solid Earth*, *118*, 6099–6112. https://doi.org/10.1002/2013JB010340

Weller, A., Breede, K., Slater, L., & Nordsiek, S. (2011). Effect of changing water salinity on complex conductivity spectra of sandstones. *Geophysics*, *76*(5), F315–F327. https://doi.org/10.1190/geo2011-0072.1

Wong, T. (1982a). Effects of temperature and pressure on failure and post-failure behavior of Westerly granite. *Mechanics of Materials*, *1*(1), 3–17. https://doi.org/10.1016/0167-6636(82)90020-5

Wong, T. (1982b). Micromechanics of faulting in westerly granite. *International Journal of Rock Mechanics and Mining Sciences*, *19*(2), 49–64. https://doi.org/10.1016/0148-9062(82)91631-X

Wong, T., & Brace, W. F. (1979). Thermal expansion of rocks: Some measurements at high pressure. *Tectonophysics*, *57*(2–4), 95–117. https://doi.org/10.1016/0040-1951(79)90143-4

Zhang, W., Sun, Q., Zhu, S., & Wang, B. (2017). Experimental study on mechanical and porous characteristics of limestone affected by high temperature. *Applied Thermal Engineering*, *110*, 356–362. https://doi.org/10.1016/j.applthermaleng.2016.08.194